CLUH controls astrin-1 expression to couple mitochondrial metabolism to cell cycle progression

Désirée Schatton[1,2], Giada Di Pietro[1,2], Karolina Szczepanowska[2,3,#], Matteo Veronese[1,2], Marie-Charlotte Marx[1,2], Kristina Braunöhler[1,2], Esther Barth[1,2], Stefan Müller[2], Patrick Giavalisco[4], Thomas Langer[2,4], Aleksandra Trifunovic[2,3,5] and Elena I. Rugarli[1,2,5*]

[1]Institute for Genetics, University of Cologne, Cologne 50931, Germany
[2]Cologne Excellence Cluster on Cellular Stress Responses in Aging-Associated Diseases (CECAD), Cologne 50931, Germany
[3] Institute for Mitochondrial Diseases and Ageing, University of Cologne, Cologne 50931, Germany
[4] Max Planck Institute for Biology of Ageing, Cologne 50931, Germany.
[5]Center for Molecular Medicine (CMMC), University of Cologne, Cologne 50931, Germany.
[#] Present address: ReMedy International Research Agenda Unit, IMol Polish Academy of Sciences, Warsaw, Poland

*Correspondence: elena.rugarli@uni-koeln.de

Abstract

Proliferating cells undergo metabolic changes in synchrony with cell cycle progression and cell division. Mitochondria provide fuel, metabolites, and ATP during different phases of the cell cycle, however it is not completely understood how mitochondrial function and the cell cycle are coordinated. CLUH is a post-transcriptional regulator of mRNAs encoding mitochondrial proteins involved in oxidative phosphorylation and several metabolic pathways. Here, we show a role of CLUH in regulating the expression of astrin, which is involved in metaphase to anaphase progression, centrosome integrity, and mTORC1 inhibition. We find that CLUH binds both the *SPAG5* mRNA and its product astrin, and controls the synthesis and the stability of the full-length astrin-1 isoform. We show that CLUH interacts with astrin-1 specifically during interphase. Astrin-depleted cells show mislocalized CLUH at focal adhesions, mTORC1 hyperactivation and enhanced anabolism. On the other hand, cells lacking CLUH show decreased astrin levels and increased mTORC1 signaling, but cannot sustain anaplerotic and anabolic pathways. In absence of CLUH, cells fail to grow during G1, and progress faster through the cell cycle, indicating dysregulated matching of growth, metabolism and cell cycling. Our data reveal a role of CLUH in coupling growth signaling pathways and mitochondrial metabolism with cell cycle progression.

39 # Introduction

40 Proliferating cells adjust their metabolism to each individual phase of the cell cycle
41 (DeBerardinis et al, 2008; Buchakjian & Kornbluth, 2010; Lee & Finkel, 2013; Salazar-Roa &
42 Malumbres, 2017). Before division cells must double their biomass and DNA content. This
43 entails a prominent rewiring of metabolism to foster biosynthetic pathways allowing the
44 synthesis of nucleic acids, proteins and lipids. During mitosis, an increase in ATP production
45 supplies the energy needed for pulling apart and segregating the chromosomes. As metabolic
46 organelles, mitochondria are key actors in the metabolic reprogramming of proliferating cells.
47 On the one hand, cell cycle regulators influence mitochondrial metabolism in various ways
48 (Leal-Esteban & Fajas, 2020). For example, CDK1 phosphorylates components of the
49 respiratory chain during G2 and of the mitochondrial translocase of the outer membrane during
50 mitosis, probably to enhance oxidative respiration and ATP production (Harbauer et al, 2014;
51 Wang et al, 2014). On the other hand, energy deficiency is sensed by cell cycle checkpoints
52 causing cell cycle arrest (Mandal et al, 2005; Salazar-Roa & Malumbres, 2017). Mitochondrial
53 dynamics is also intimately linked to cell cycle progression. A hyperfused mitochondrial
54 network is important for the G1-S transition, while mitochondria must fragment before cells
55 enter mitosis (Mitra et al, 2009). Therefore, proliferating cells depend on several coordinated
56 mechanisms to regulate how mitochondria utilize nutrients to fuel cell growth or energy
57 production during the cell cycle. However, how mitochondrial metabolism and respiratory
58 function are coordinated during the cell cycle is still largely unclear. Unravelling these
59 mechanisms is crucial since they are often dysregulated in cancer.

60 One of the ways how mitochondrial metabolism can be rewired is through regulation of RNA
61 regulons by RNA-binding proteins (Schatton & Rugarli, 2018). CLUH (clustered mitochondria
62 homologue) is a conserved RNA-binding protein, which binds transcripts encoding proteins
63 involved in the respiratory chain, the TCA cycle, and other mitochondrial metabolic pathways

64 (Gao et al, 2014). Upon loss of CLUH, target mRNAs are subjected to faster decay and their
65 respective proteins are decreased in abundance (Schatton et al, 2017). This leads to alterations
66 in mitochondrial distribution (mitochondrial clustering as the gene name alludes to)
67 mitochondrial cristae integrity, respiratory defects, loss of mtDNA, and decreased activity of
68 TCA cycle enzymes (Schatton et al, 2017; Wakim et al, 2017; Pla-Martin et al, 2020). In the
69 mouse, constitutive loss of *Cluh* causes neonatal lethality, while a liver-specific *Cluh* knock-
70 out (KO) led to hypoglycemia and defective ketogenesis upon starvation (Schatton et al, 2017).
71 CLUH and its target mRNAs form ribonucleoprotein particles in primary hepatocytes. These
72 CLUH granules are important not only to protect target mRNAs from degradation, but also to
73 restrict mTORC1 activation and promote mitophagy (Pla-Martin et al, 2020). Thus, in post-
74 mitotic hepatocytes CLUH controls the balance between catabolism and anabolism, allowing a
75 survival response to starvation.

76 Astrin (also called SPAG5) is a multifunctional protein with a well-established role during
77 mitosis. The complex astrin/kinastrin/DYNLL1 is involved in the stabilization of the
78 kinetochore-microtubule interactions in metaphase (Kern et al, 2017). Consistently, cells
79 lacking astrin or its interactor kinastrin show defects in chromosome segregations and a delayed
80 metaphase to anaphase progression (Gruber et al, 2002; Dunsch et al, 2011). Astrin has however
81 other roles in interphase, ranging from mTORC1 inhibition (Thedieck et al, 2013), centrosome
82 integrity and centriole duplication (Thein et al, 2007; Kodani et al, 2015), and regulation of p53
83 levels during G2 after DNA damage (Halim et al, 2013). Astrin is highly expressed in several
84 cancers and it is considered a poor prognostic marker (Yuan et al, 2014; Abdel-Fatah et al,
85 2016; Bertucci et al, 2016; Zhou et al, 2018; Ying et al, 2020).

86 We show here that in HeLa cells astrin exists in two isoforms, astrin-1 and astrin-2. We reveal
87 that CLUH binds the *SPAG5* mRNA, as well as the astrin-1 protein. The interaction of CLUH
88 and astrin-1 occurs during interphase and protects astrin-1 and kinastrin from degradation.

89 Moreover, we show that CLUH positively regulates mitochondrial anaplerotic pathways that
90 sustain mTORC1 activation. Our data disclose a role of CLUH in coupling mitochondrial
91 metabolism to cell cycle progression.

92 Results

93 CLUH interacts with astrin-1 and kinastrin

94 We previously showed that CLUH binds several mRNAs for mitochondrial proteins (Gao et al,
95 2014). However, among CLUH-bound transcripts, we found *SPAG5* encoding astrin, a
96 multifunctional protein involved in metaphase to anaphase progression, centrosome integrity
97 and mTORC1 regulation (Gruber et al, 2002; Thein et al, 2007; Schmidt et al, 2010; Dunsch et
98 al, 2011; Thedieck et al, 2013; Gao et al, 2014; Kodani et al, 2015). Surprisingly, we also
99 detected astrin as an RNA-independent interactor of endogenous CLUH in a pull-down
100 experiment in HeLa cells after stable isotope labeling in cell culture (SILAC) followed by mass
101 spectrometry (Supplementary Table 1). Reciprocal immunoprecipitations (IPs) using
102 antibodies against human CLUH and astrin, followed by western blot, confirmed the interaction
103 (Figure 1A). Binding was also validated between CLUH and kinastrin (also known as SKAP),
104 a known astrin interactor (Figure 1B) (Schmidt et al, 2010; Dunsch et al, 2011).
105 Astrin appears as two isoforms (hereafter referred to as astrin-1 and astrin-2) in western blots,
106 and CLUH interacts preferentially with the slower migrating isoform, astrin-1 (Figure 1A). The
107 existence of these two isoforms has been reported in the literature but their identity remains
108 enigmatic. On closer inspection of the *SPAG5* mRNA, we noticed the presence of five in-frame
109 ATGs downstream of the first ATG (hereafter referred to as ATG2-6), which could serve as
110 alternative translation start codons (with moderate and good Kozak sequences) (Figure 1C).
111 Moreover, an upstream ORF within the *SPAG5* 5' UTR (Figure 1C) could influence translation
112 from the downstream ATGs as reported for other genes (Morris & Geballe, 2000; Young &

113 Wek, 2016). To test these hypotheses, we produced different constructs expressing the 5' UTR
114 and the coding region of the *SPAG5* cDNA, and we mutagenized the uATG, the ATG1 or
115 downstream ATGs individually or in different combinations to GGG (Figure 1-figure
116 supplement 1A). When we expressed the uATG^{GGG}-SPAG5 construct, the expression of astrin-
117 2 was suppressed (Figure 1D). Furthermore, mutagenesis of ATG1 confirmed the existence of
118 a downstream alternative translation start site (Figure 1D). Overexpression of the constructs
119 harboring mutagenized downstream ATGs revealed that astrin-2 is the product of alternative
120 translation starting from ATG3-5 (Figure 1E). The identity of astrin-1 was also confirmed by
121 pull-down of this isoform only using an antibody directed against the N-terminal region of the
122 protein (Figure 1-figure supplement 1B).

123 To evaluate whether the interaction domain of astrin that binds to CLUH lies in the N-terminal
124 part of astrin-1, we transfected a construct expressing both astrin-1 and astrin-2 (ATG1-SPAG5,
125 Figure 1-figure supplement 1A) or an N-terminus deleted variant (Δ151-SPAG5, Figure 1-
126 figure supplement 1A) and performed reciprocal IPs in HeLa wildtype and *CLUH* KO cells
127 (Wakim et al, 2017) (Figure 1F). An interaction was observed only with full-length astrin,
128 proving that CLUH binds within the N-terminus of astrin-1 (Figure 1F). In contrast, the astrin
129 interactor kinastrin has no binding preference to any of the two astrin isoforms, consistent with
130 the previously mapped interaction domain between these two proteins (residues 482-693 of
131 astrin) (Figure 1-figure supplement 1C) (Dunsch et al, 2011; Friese et al, 2016; Kern et al, 2016;
132 Kern et al, 2017). CLUH still interacts with astrin-1 upon kinastrin depletion, suggesting that
133 kinastrin is not required for the interaction (Figure 1-figure supplement 1D). In polysome
134 profiles performed after chemical crosslinking, CLUH migrated in lighter fractions, as well as
135 in fractions containing the monosome and polysomes (Figure 1G). In contrast, astrin and
136 kinastrin were only detected in the lighter fractions (Figure 1G).

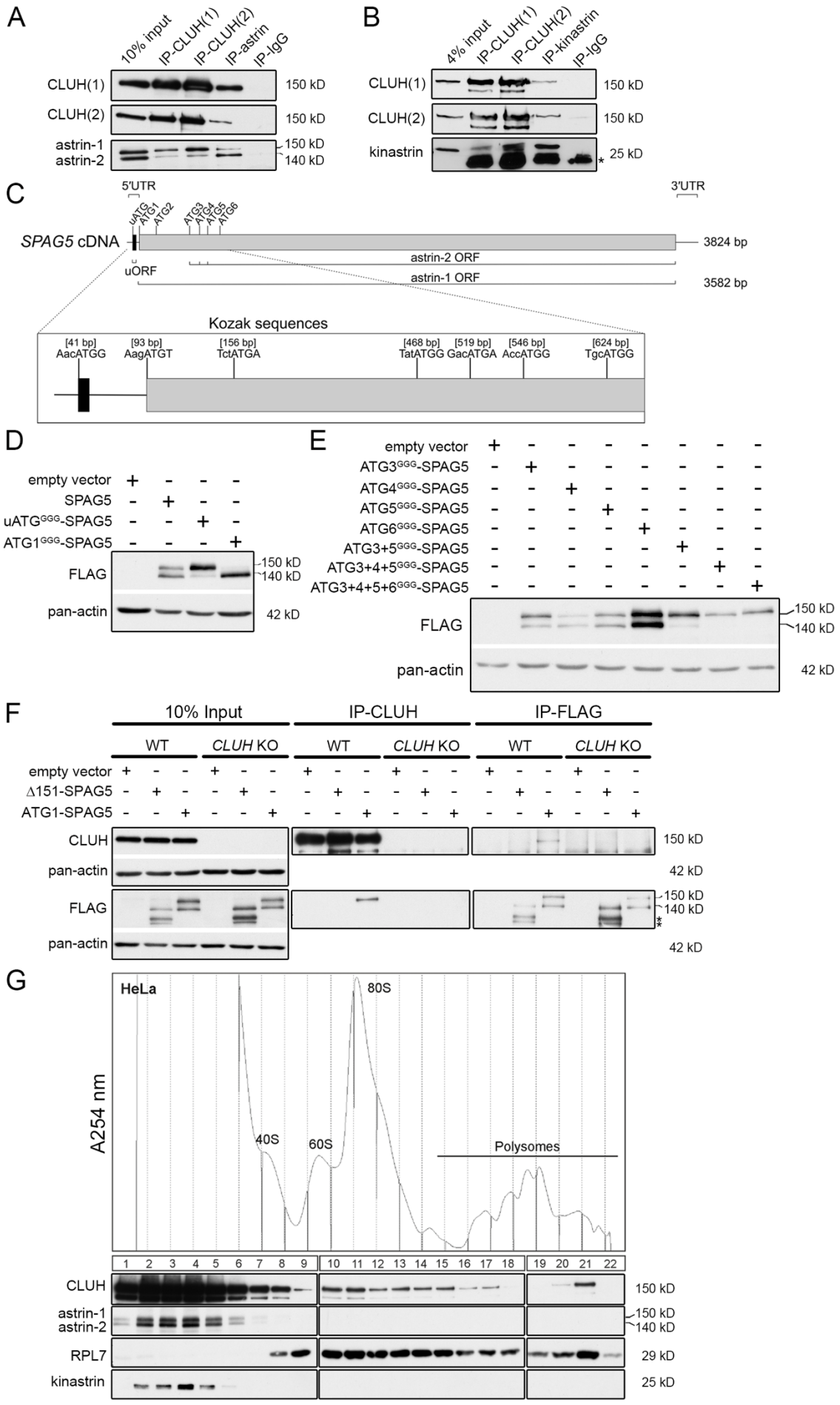
A
10% input
IP-CLUH(1)
IP-CLUH(2)
IP-astrin
IP-IgG
CLUH(1)
CLUH(2)
astrin-1
astrin-2
150 kD
150 kD
150 kD
140 kD
B
4% input
IP-CLUH(1)
IP-CLUH(2)
IP-kinastrin
IP-IgG
CLUH(1)
CLUH(2)
kinastrin
150 kD
150 kD
25 kD
C
5'UTR
3'UTR
uATG
ATG1
ATG2
ATG3
ATG4
ATG5
ATG6
SPAG5 cDNA
3824 bp
uORF
astrin-2 ORF
astrin-1 ORF
3582 bp
Kozak sequences
[41 bp] AacATGG
[93 bp] AagATGT
[156 bp] TctATGA
[468 bp] TatATGG
[519 bp] GacATGA
[546 bp] AccATGG
[624 bp] TgcATGG
D
empty vector
SPAG5
uATG^GGG-SPAG5
ATG1^GGG-SPAG5
FLAG
pan-actin
150 kD
140 kD
42 kD
E
empty vector
ATG3^GGG-SPAG5
ATG4^GGG-SPAG5
ATG5^GGG-SPAG5
ATG6^GGG-SPAG5
ATG3+5^GGG-SPAG5
ATG3+4+5^GGG-SPAG5
ATG3+4+5+6^GGG-SPAG5
FLAG
pan-actin
150 kD
140 kD
42 kD
F
10% Input
IP-CLUH
IP-FLAG
WT
CLUH KO
empty vector
Δ151-SPAG5
ATG1-SPAG5
CLUH
pan-actin
FLAG
pan-actin
150 kD
42 kD
150 kD
140 kD
42 kD
G
HeLa
80S
40S
60S
Polysomes
A254 nm
1 2 3 4 5 6 7 8 9 10 11 12 13 14 15 16 17 18 19 20 21 22
CLUH
astrin-1
astrin-2
RPL7
kinastrin
150 kD
150 kD
140 kD
29 kD
25 kD

137

138 **Figure 1. CLUH interacts with astrin-1 and kinastrin.**
139 (**A, B**) Western blots of reciprocal co-IPs of endogenous CLUH, astrin and kinastrin in HeLa cells. Two
140 different antibodies have been used to pull down CLUH (1, 2). Asterisks mark IgG light chain. (**C**)
141 Scheme of human *SPAG5* cDNA with indicated UTRs and ORFs. Close up shows positions of the uATG
142 and ATG1-6 with surrounding Kozak sequences. (**D, E**) Western blots of HeLa cells overexpressing
143 FLAG-tagged astrin constructs. Pan-actin was used as loading control. (**F**) Western blots of reciprocal
144 co-IPs of endogenous CLUH and overexpressed FLAG-tagged astrin full length (ATG1-SPAG5) or a
145 N-terminal deleted variant (Δ151-SPAG5) in WT and *CLUH* KO HeLa cells. Pan-actin was used as
146 loading control for input samples. Asterisks indicate additional astrin bands appearing upon
147 overexpression of the N-terminal deleted variant. (**G**) Polysome profiling of HeLa cells chemically
148 crosslinked with DSP. At the top, absorbance profile at 254 nm of the fractions is shown with indicated
149 peaks of 40S and 60S ribosomal subunits, 80S monosome and polysomes; at the bottom the
150 corresponding western blots of the fractions are shown. RPL7 was used as a marker for ribosomes.
151

152 In conclusion, we identify the expression of two astrin isoforms via alternative initiation of
153 translation, and establish CLUH as a specific molecular partner of astrin-1.

154 CLUH controls astrin-1 and kinastrin stability and astrin expression

155 In absence of CLUH, kinastrin and astrin-1, but not astrin-2, are decreased in abundance (Figure
156 2A). To investigate whether CLUH influences the stability of its interaction partners, we
157 performed a cycloheximide (CHX) chase in wildtype and *CLUH* KO HeLa cells (Figure 2A).
158 In absence of CLUH, kinastrin and astrin-1, but not astrin-2, are highly unstable (Figure 2A-
159 D). The instability of astrin in absence of CLUH was confirmed in *Cluh* KO MEFs which only
160 express the larger isoform of astrin (Figure 2-figure supplement 1A, B). Inhibition of the
161 proteasome by MG132 treatment in *CLUH* KO HeLa cells fully rescued kinastrin and partially
162 astrin-1 levels (Figure 2A, E-G). Decreased kinastrin levels upon astrin depletion have already
163 been reported (Schmidt et al, 2010; Dunsch et al, 2011).

164 The underlying reason for the only partial rescue of astrin-1 might be another level of regulation
165 by CLUH. Given the identification of *SPAG5* mRNA as a CLUH target (Gao et al, 2014), we
166 tested if CLUH is involved in astrin synthesis. To this end, we immunoprecipitated newly

167 synthesized astrin in wildtype and *CLUH* KO cells after labeling with ^{35}S methionine for
168 different time points (Figure 2H-I). We observed that CLUH regulates the synthesis of astrin-
169 1 (Figure 2H-I). CLUH controls the expression of some of its target mRNAs by preventing their
170 degradation (Schatton et al., 2017). To elucidate whether this is also the case for *SPAG5*, we
171 labeled newly synthesized RNA with the uridine analog ethynyl uridine (EU) and chased it for
172 8 h. We precipitated the EU-RNA with biotin-azide using Click-iT chemistry and quantified
173 *SPAG5* mRNA levels with qRT-PCR. *SPAG5* mRNA was less stable in absence of CLUH,
174 whereas steady state levels and EU incorporation were unaffected (Figure 2J-L).

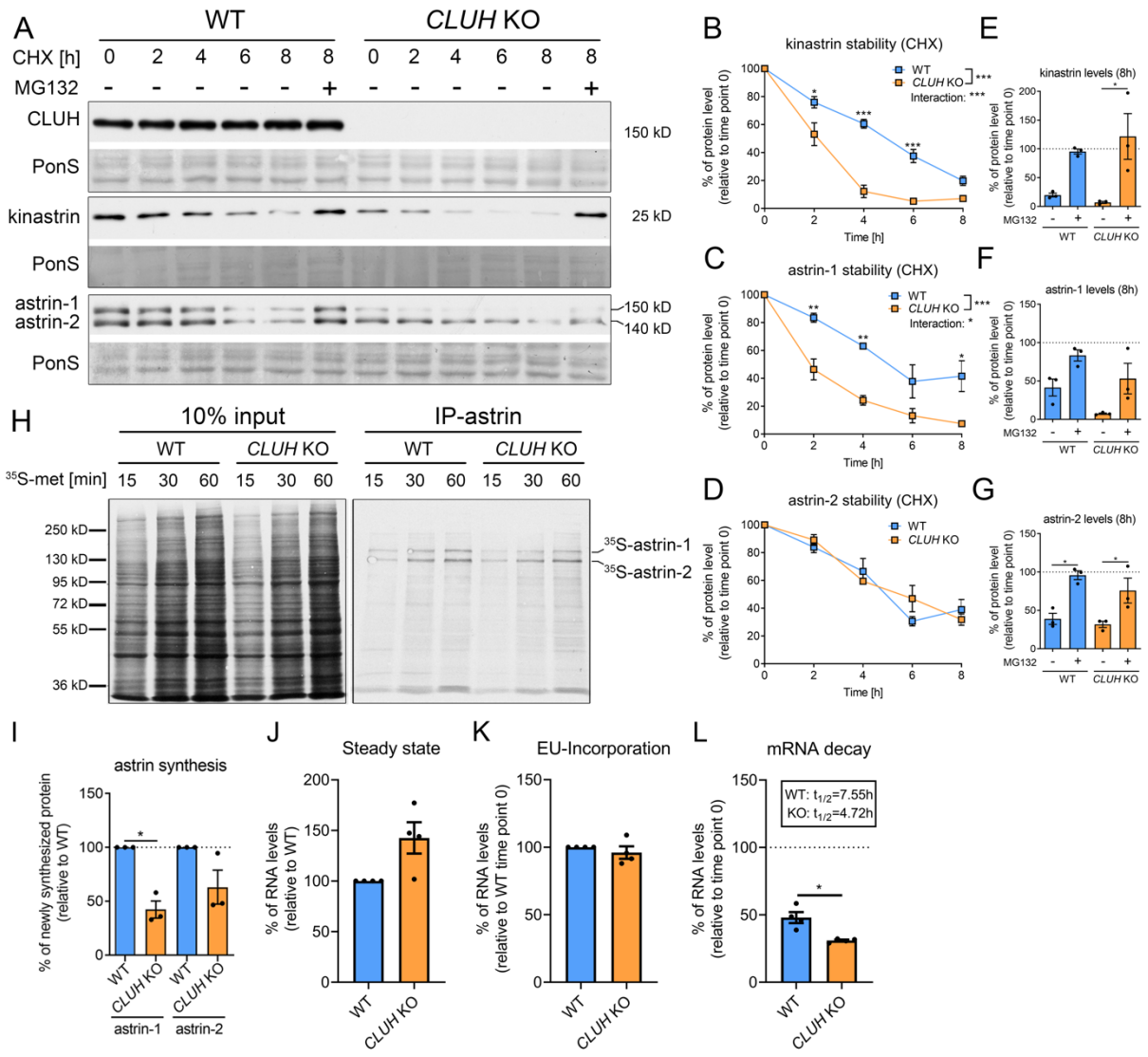

175

176 **Figure 2. CLUH controls astrin-1 and kinastrin stability and astrin expression.**

177 (**A**) Western blots of WT and *CLUH* KO HeLa cells treated with CHX for indicated time points with or
178 w/o additional MG132 treatment. Ponceau S staining was used as loading control. (**B-D**) Quantification
179 of CHX chase western blots as shown in A (n=3 independent experiments). Two-way ANOVA with
180 post hoc Tukey`s multiple comparison tests were performed with P≤0.05: *; P≤0.01: **; P≤0.001: ***.
181 Genotype x time interaction significance is also shown. Error bars represent SEM. (**E-G**) Quantification
182 of proteins levels after 8 h CHX treatment of western blots as shown in A (n=3 independent
183 experiments). Bars show the mean ± SEM. Dotted lines indicate protein levels at 0h time points. One-
184 way ANOVA with post hoc Tukey`s multiple comparison tests were performed with P≤0.05: *. (**H**)
185 Autoradiograms of IP of newly synthesized astrin labeled with ^{35}S-methionine for indicated time points
186 in WT and *CLUH* KO HeLa cells. (**I**) Quantification of immunoprecipitated newly synthesized astrin
187 after 60 min labeling of experiments as shown in H (n=3 independent experiments). Bars show the mean
188 ± SEM. Two-tailed paired Student's t-test was performed with P≤0.05: *. (**J**) Steady state mRNA levels
189 of *SPAG5* in WT and *CLUH* KO HeLa cells (n=4 independent experiments). Bars show mean ± SEM.
190 *RPL13* levels have been used for normalization. (**K, L**) Levels of EU-incorporation (K) and mRNA
191 decay (L) of *SPAG5* mRNA in WT and *CLUH* KO HeLa cells after specific labeling and pull down of
192 newly synthesized RNA (n=4 independent experiments). *GAPDH* levels have been used for
193 normalization. Calculated half-lives are indicated. Bars show the mean ± SEM. Two-tailed paired
194 Student's t-test was performed with P≤0.05: *.

195 In conclusion, our data reveal that CLUH controls the expression of astrin-1 at multiple levels,
196 by binding and stabilizing its mRNA, by affecting its synthesis, and maintaining its stability.

197 CLUH binds astrin-1 in interphase

198 Astrin controls cell cycle progression at various stages, raising the question if the complex
199 CLUH-astrin-1 is cell cycle-dependent. To this end, we immunoprecipitated CLUH from cells
200 enriched in different phases of the cell cycle (Figure 3A, Figure 3-supplement 1A). The
201 effective synchronization of the cells was confirmed by analyzing the input levels of cyclin D3
202 (G2 phase marker), pH3-Ser10 (M phase marker) and pRPS6-Ser235/236 (inhibited upon
203 starvation) (Figure 3A). Astrin-1, but not astrin-2, was more abundant in S and G2, while CLUH
204 levels were similar in the different phases of the cell cycle (Figure 3A). Both astrin isoforms
205 are phosphorylated at multiple sites, leading to slower migration in SDS-PAGE in
206 prometaphase (PM) (Figure 3A) (Chang et al, 2001; Cheng et al, 2008; Chiu et al, 2014; Chung

207 et al, 2016; Geraghty et al, 2021). The CLUH/astrin-1 complex is enriched in S and G2 phases
208 but not detected in PM, indicating that CLUH preferentially interacts with unmodified astrin-1
209 in interphase and that the interaction might be controlled by the phosphorylation status of astrin
210 (Figure 3A).
211

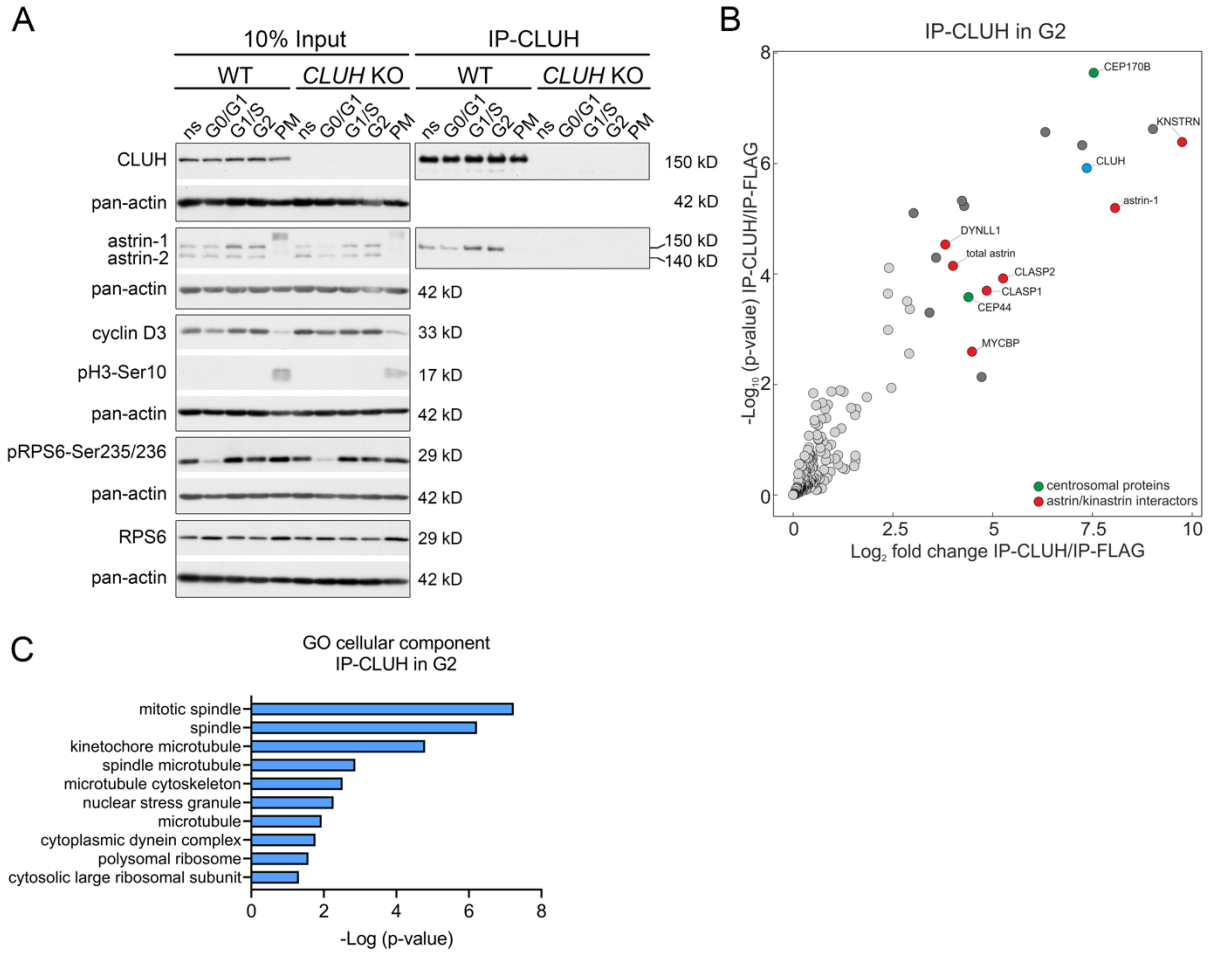

212

213 **Figure 3. The astrin-1/CLUH complex is enriched in interphase.**
214 (**A**) Western blots of co-IPs of endogenous CLUH in WT and *CLUH* KO HeLa cells. Cells have been
215 synchronized as shown in Figure 3-figure supplement 1A. Pan-actin was used as loading control and
216 cyclin D3 as G2 phase marker, pH3-Ser10 as M phase marker and pRPS6-Ser235/236 to assess effective
217 starvation of input samples. (**B**) Enriched proteins immunoprecipitated with an antibody against
218 endogenous CLUH in G2-synchronized HeLa cells and detected by mass spectrometry (n=4
219 independent replicates). Highlighted are all proteins enriched with a log2FC ≥3 and q≤0.05. Marked in
220 green are centrosomal proteins; marked in red are previously identified astrin/kinastrin interactors. (**C**)
221 GO cellular component analysis of enriched proteins highlighted in B analyzed using the EnrichR
222 webtool.
223

224 To fully capture the CLUH interactome, we performed four biological independent IPs of
225 CLUH in G2-synchronized wildtype cells followed by label-free mass spectrometry (Figure
226 3B, Figure 3-figure supplement 1A). The correct synchronization was confirmed by propidium
227 iodide (PI) staining followed by flow cytometry (Figure 3-figure supplement 1B, C). This
228 experiment confirmed astrin-1 and kinastrin as highly enriched interactors of CLUH (Figure
229 3B and Supplementary Table 2). In addition, proteins previously shown to be part of the
230 astrin/kinastrin complex, such as MYCBP, or linking the complex to the microtubule
231 cytoskeleton were also detected in the precipitate. Among these proteins are CLASP1 and 2,
232 two microtubule plus-end binding proteins, and DYNLL1, a retrograde motor protein (Manning
233 et al, 2010; Schmidt et al, 2010; Dunsch et al, 2011; Kern et al, 2016; Kern et al, 2017) (Figure
234 3B). Interestingly, among top CLUH interactors, we found the centrosomal proteins CEP170B
235 and CEP44, indicating a link of CLUH with the centrosome and the microtubules (Figure 3B,
236 C).

237 Astrin-1 regulates the subcellular localization of CLUH

238 The previous data strongly indicate the existence of a pool of CLUH that interacts with
239 microtubular structures, including centrosomes. We tested the role of astrin-1 in defining the
240 subcellular localization of CLUH. Overexpression of astrin-1, but not of astrin-2, recruited
241 endogenous CLUH to a perinuclear formation (Figure 4A). These formations are γ-tubulin
242 positive (Figure 4B, C), in line with the reported localization of astrin to the centrosome and
243 the pericentriolar region (Cheng et al, 2007; Thein et al, 2007; Kodani et al, 2015). To
244 substantiate the hypothesis that astrin-1 controls CLUH subcellular localization, we derived a
245 monoclonal cell line completely devoid of astrin expression (referred to as *SPAG5* KO) (Figure
246 4D). CLUH staining was overtly different in these cells, showing a characteristic accumulation
247 in peripheral granular structures in a high percentage of cells (Figure 4E, F). These structures
248 were also positive for vinculin, a marker of focal adhesions (Figure 4E). These findings are

249 consistent with a role of astrin-1 in regulating the localization to the centrosomes of a pool of

250 CLUH.

251

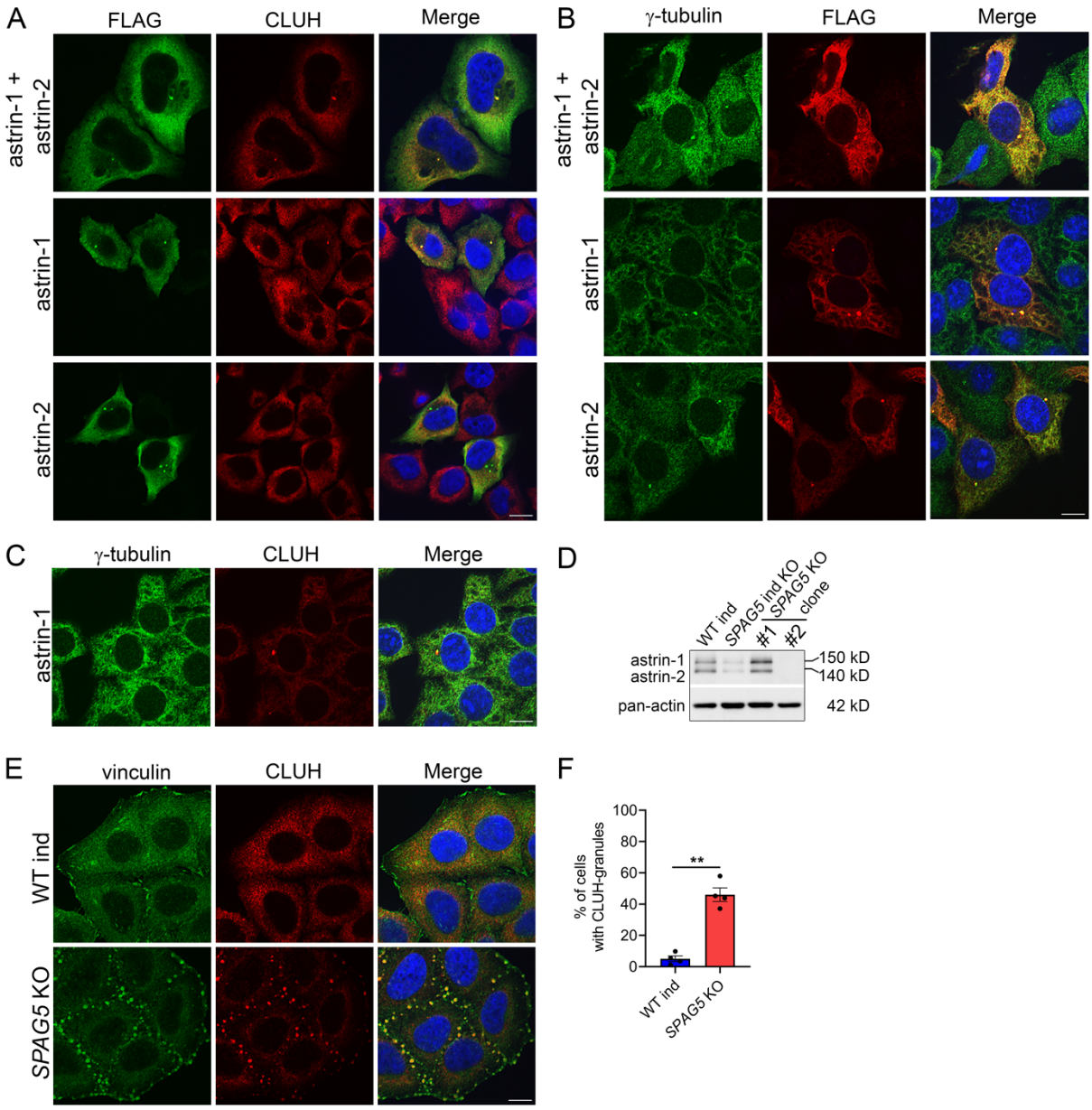

252

253 **Figure 4. Astrin-1 controls CLUH subcellular localization.**

254 (**A-C**) Confocal immunofluorescence pictures of HeLa cells overexpressing FLAG-tagged astrin-1 and
255 astrin-2 (SPAG5), astrin-1 (ATG3+4+5^{GGG}-SPAG5) or astrin-2 (ATG1^{GGG}-SPAG5) alone stained for
256 FLAG (green) and CLUH (red) (A) or γ-tubulin (green) and FLAG (red) (B) or γ-tubulin (green) and
257 CLUH (red) (C). DAPI was used to stain nuclei (blue). Cells were fixed with 4%PFA/PBS (A) or ice-
258 cold methanol (B, C). Scale bar, 10 µm. (**D**) Western blots of WT and *SPAG5* KO HeLa clones. Pan-
259 actin was used as loading control. *SPAG5* KO clone #2 has been used for experiments in this study. (**E**)
260 Confocal immunofluorescence pictures of WT ind and *SPAG5* KO HeLa cells stained for vinculin

261 (green) and CLUH (red). DAPI was used to stain nuclei (blue). Scale bar, 10 µm. (**F**) Quantification of
262 cells with CLUH-granules of experiments as shown in E (n=4 independent experiments). Bars show
263 mean ± SEM and dots represent values of individual replicates. At least 160 cells per genotype per
264 replicate have been counted. Two-tailed paired Student's t-test was performed with P≤0.01: **.
265

266 Loss of astrin or kinastrin do not recapitulate CLUH-dependent 267 mitochondrial phenotypes

268 What is the function of CLUH in complex with astrin-1 and kinastrin? We first asked whether
269 loss of astrin or kinastrin phenocopies CLUH-dependent mitochondrial abnormalities. To avoid
270 possible compensatory effects in stable KO clones, we employed inducible CRISPR-Cas9
271 astrin and kinastrin KO HeLa cells (hereafter referred to as *SPAG5* and *KNSTRN* ind-KO) in
272 which there is constant expression of sgRNAs complementary to the target genes and the
273 expression of the Cas9 is doxycycline inducible (Kern et al, 2017; McKinley & Cheeseman,
274 2017). Using this system, we induced an acute deletion of astrin and kinastrin for four days, in
275 many but not all cells (Figure 5-figure supplement 1A, B). We focused on previously reported
276 phenotypes observed in *CLUH* KO cells or tissues, such as mitochondrial clustering,
277 mitochondrial fragmentation, loss of mtDNA, and decreased assembled respiratory complexes
278 (Gao et al, 2014; Schatton et al, 2017; Wakim et al, 2017). Mitochondrial distribution,
279 morphology, ultrastructure and mtDNA levels were indistinguishable in WT, *SPAG5* and
280 *KNSTRN* ind-KO cells (Figure 5A-C, Figure 5-figure supplement 1C-E). Furthermore,
281 respiratory supercomplexes containing complex I and III assembled normally in these cells, and
282 in-gel activity of complex I was similar to control cells (Figure 5D). In contrast, cells lacking
283 CLUH displayed a reduction of assembled supercomplexes I-III, decreased activity of complex
284 I, and abnormal mitochondrial ultrastructure (Figure 5D and Figure 5-figure supplement 1E).
285 These data indicate that CLUH controls mitochondrial function independent from the
286 interaction with astrin-1 or kinastrin.

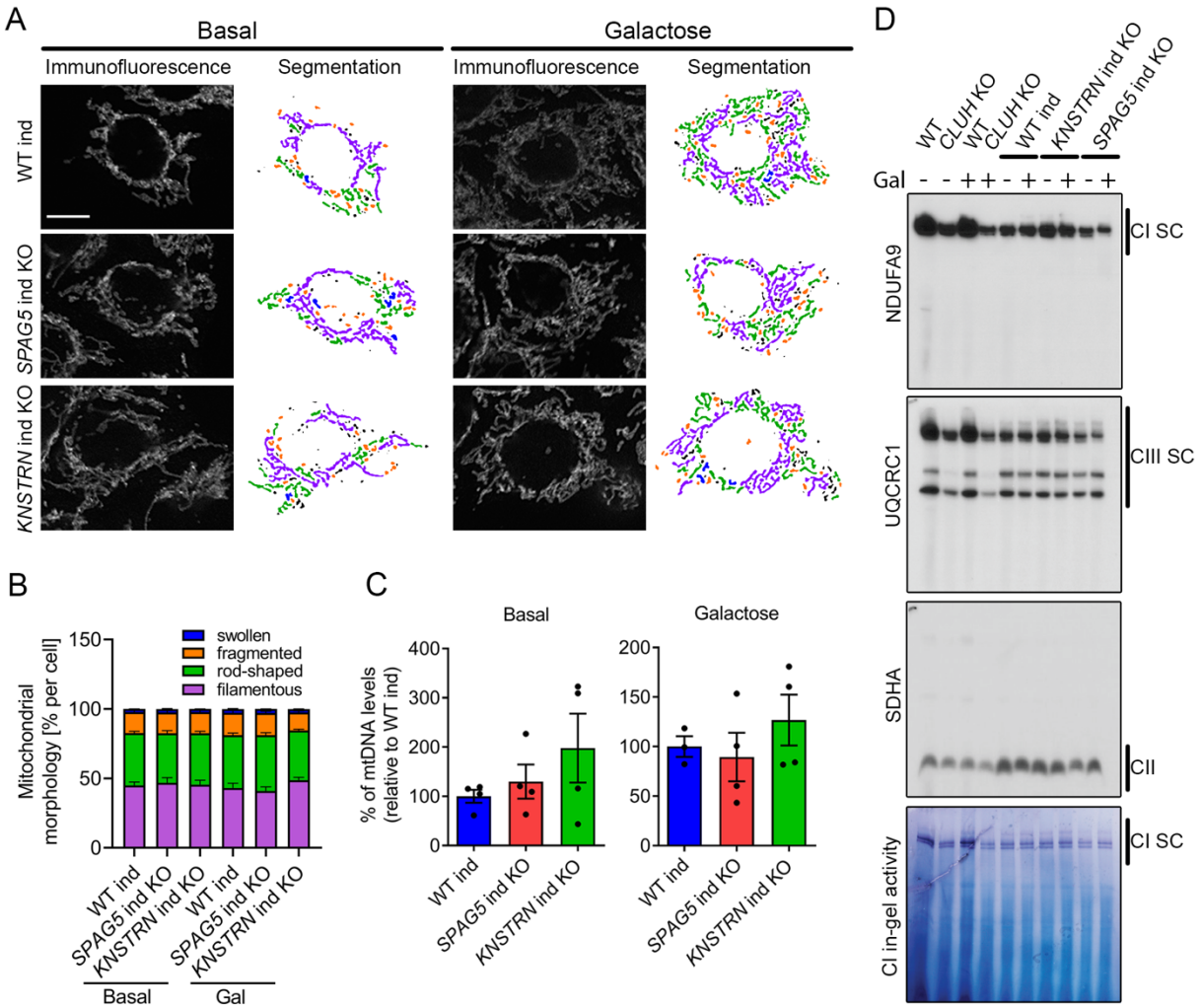

Figure 5. Astrin and kinastrin depletion does not mimic mitochondrial phenotypes seen upon absence of CLUH.

(**A**) Mitochondrial network of WT, *SPAG5* and *KNSTRN* ind-KO HeLa cells grown in basal or galactose media for 16 h. Mitochondria were stained with an antibody against TOMM20. Scale bar, 10 µm. On the left side, confocal immunofluorescence pictures are shown, on the right side, mitochondrial network is shown after segmentation. Color code for different mitochondrial morphologies: purple: filamentous; green: rod-shaped; orange: fragmented; blue: swollen; black: unclassifiable. (**B**) Quantification of mitochondrial morphology of experiments as shown in A (n=3 independent experiments; at least 66 in basal or 44 cells in galactose have been analyzed per genotype per replicate). Bars show the mean of each morphological class with SEM. (**C**) mtDNA levels of WT, *SPAG5* and *KNSTRN* ind-KO HeLa cells grown in basal or galactose media for 16 h (n=4 independent experiments). Bars show mean ± SEM and dots represent values of individual replicates. (**D**) BN-PAGE analysis of respiratory chain supercomplexes and complex I activity staining of isolated mitochondria of WT, *CLUH* KO and WT, *SPAG5* and *KNSTRN* ind-KO HeLa cells grown in basal or galactose media for 16 h.

304 **Loss of astrin rewires metabolic pathways to promote anabolism**

305 To define how astrin and kinastrin affect cell function, we performed label free quantitative
306 proteomics in *SPAG5* and *KNSTRN* ind-KO cells. In line with the short time of induced KOs,
307 only minor differences in the overall proteome in *SPAG5* and *KNSTRN* ind-KO cells compared
308 to ind-WT cells was observed (Figure 6A and Supplementary Table 3). Notably, CLUH levels
309 were unaffected by the loss of its interactors (Figure 6A and Supplementary Table 3). Astrin
310 depletion caused a slight decrease of proteins encoded by CLUH mRNA targets (Figure 6A;
311 marked in blue). Downregulated KEGG pathways, analyzed using the EnrichR webtool (using
312 a generous cut-off of $p \leq 0.05$; $q \leq 0.15$) (Chen et al, 2013; Kuleshov et al, 2016; Xie et al, 2021),
313 largely overlapped with metabolic pathways affected by CLUH deletion (TCA cycle, fatty acid
314 and amino acid degradation; Figure 6B) (Schatton et al, 2017). Interestingly, metabolic
315 pathways connected to nucleotide biosynthesis (purine and pyrimidine metabolism), the
316 pentose phosphate pathway (PPP) and glycolysis were upregulated (Figure 6C). Furthermore,
317 mTORC1 appeared as one of the most enriched terms in pathway analysis of perturbed proteins
318 (Figure 6-figure supplement 1A, B).

319 The proteomic profile of *SPAG5* ind-KO cells is consistent with a previous study that identified
320 astrin as a negative regulator of mTORC1 (Thedieck et al, 2013). We confirmed that mTORC1
321 is hyperactive in *SPAG5* ind-KOs upon starvation for 8 h in HBSS (Figure 6-figure supplement
322 1C, D). To reveal if this increased signaling is reflected in cell metabolism, we performed
323 targeted metabolomics analysis in *SPAG5* and *KNSTRN* ind-KO cells.

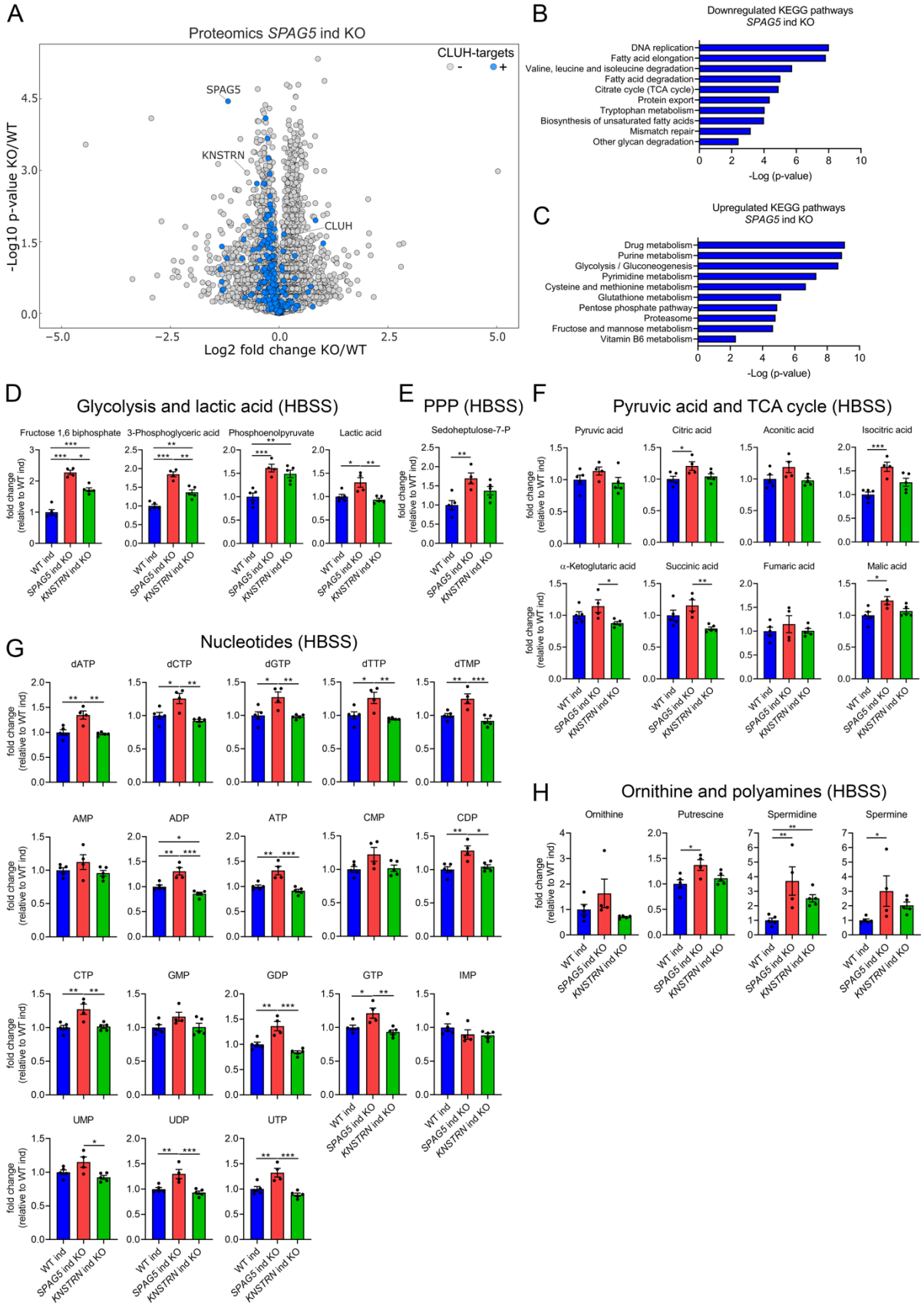

Figure 6. Astrin loss promotes anabolic pathways.

326 (**A**) Volcano plot of label-free proteomics of WT and *SPAG5* ind KO HeLa cells (n=4 independent
327 replicates). CLUH targets are marked in blue. (**B, C**) KEGG pathways of downregulated (B) or
328 upregulated (C) proteins (with a cut-off of p≤0.05; q≤0.15) detected in proteomics analysis of *SPAG5*
329 ind-KO cells (A and Supplementary Table3) using the EnrichR webtool. (**D-H**) Targeted metabolomics
330 of WT, *SPAG5* and *KNSTRN* ind-KO cells after 8 h HBSS starvation showing glycolytic intermediates
331 and lactic acid (D), sedoheptulose-7-P (E), pyruvic acid and TCA cycle intermediates (F), nucleotide
332 levels (G) and ornithine and polyamine levels (H). Bars show mean ± SEM and dots represent values of
333 individual replicates. One-way ANOVA with post hoc Tukey`s multiple comparison tests on log
334 converted fold changes were performed with P≤0.05: *; P≤0.01: **; P≤0.001: ***.
335
336 In agreement with the mild proteomics changes, metabolomics of *SPAG5* ind-KO under basal
337 condition did not reveal major alterations of the pools of glycolytic and TCA cycle
338 intermediates, amino acids, and nucleotides, with the exception of an increase in glutamine,
339 proline, lactate, and citric acid (Figure 6-figure supplement 2A-E). Upon starvation, *SPAG5*
340 depletion led to more prominent alterations of the metabolome, with accumulation of several
341 glycolytic intermediates, lactate, and sedoheptulose-7-phosphate, in agreement with high
342 glycolytic rate and an increase in the PPP (Figure 6D, E). In addition, the TCA cycle
343 intermediates citrate, isocitrate and malate were increased (Figure 6F). Both the TCA cycle and
344 the PPP intermediates are crucial for synthesis of nucleotides, several of which accumulated in
345 astrin-deficient cells (Figure 6G). Amino acid levels were unaffected (Figure 6-figure
346 supplement 2F), with the exception of an increase of ornithine, a precursor of polyamines,
347 which were also more abundant (Figure 6H). *KNSTRN* ind-KO cells did not show detectable
348 metabolic differences to control cells (Figure 6D-H and Figure 6-figure supplement 2A-F).
349 Together, our data show that cells depleted of astrin, despite starvation, engage in anabolic
350 pathways linked to cell growth, in agreement with hyperactivated mTORC1 signaling.

351 Loss of CLUH impairs anaplerotic and anabolic pathways

352 Increased mTORC1 signaling upon starvation is also a prerogative of CLUH-deficient cells and
353 tissues (Pla-Martin et al, 2020) (Figure 6-figure supplement 1C, D). Surprisingly, the metabolic

354 profile of starved *CLUH* KO cells was strikingly different from that of *SPAG5* ind-KO cells
355 (Figure 7A-F). Targeted metabolomics revealed a prominent decrease of the PPP intermediate
356 sedoheptulose-7-phosphate, and a significant increase of pyruvate (Figure 7A-C). The
357 intermediates of the first part of the TCA cycle (citrate, aconitate, and isocitrate) were decreased
358 (Figure 7C). In addition, most amino acids that feed into the TCA cycle were decreased (Figure
359 7D), including aspartate, which is mainly produced by oxaloacetate and is an important
360 precursor of pyrimidines (Figure 7D). Glutamine was instead elevated, as well as α-
361 ketoglutarate (Figure 7C, D). In addition, cells lacking CLUH showed a perturbation of
362 polyamines metabolism, with a prominent reduction of spermidine, and decreased levels of
363 some nucleotides, especially inosine monophosphate (IMP), the first nucleotide in the synthesis
364 pathway of purines (Figure 7E, F). Thus, upon starvation *CLUH* KO cells fail to maintain the
365 TCA cycle intermediates (anaplerosis), and surprisingly show defects also in other anabolic
366 pathways that are linked to cell growth and are regulated by mTORC1. This metabolic profile
367 is strikingly opposite to that of *SPAG5* ind-KO cells, and indicate that the mTORC1
368 hyperactivation in absence of CLUH is not reflected in the cellular metabolic rewiring. This
369 data points to an important role of CLUH in the mTORC1-dependent rewiring of cellular
370 metabolism, by supporting mitochondrial anaplerotic pathways.
371

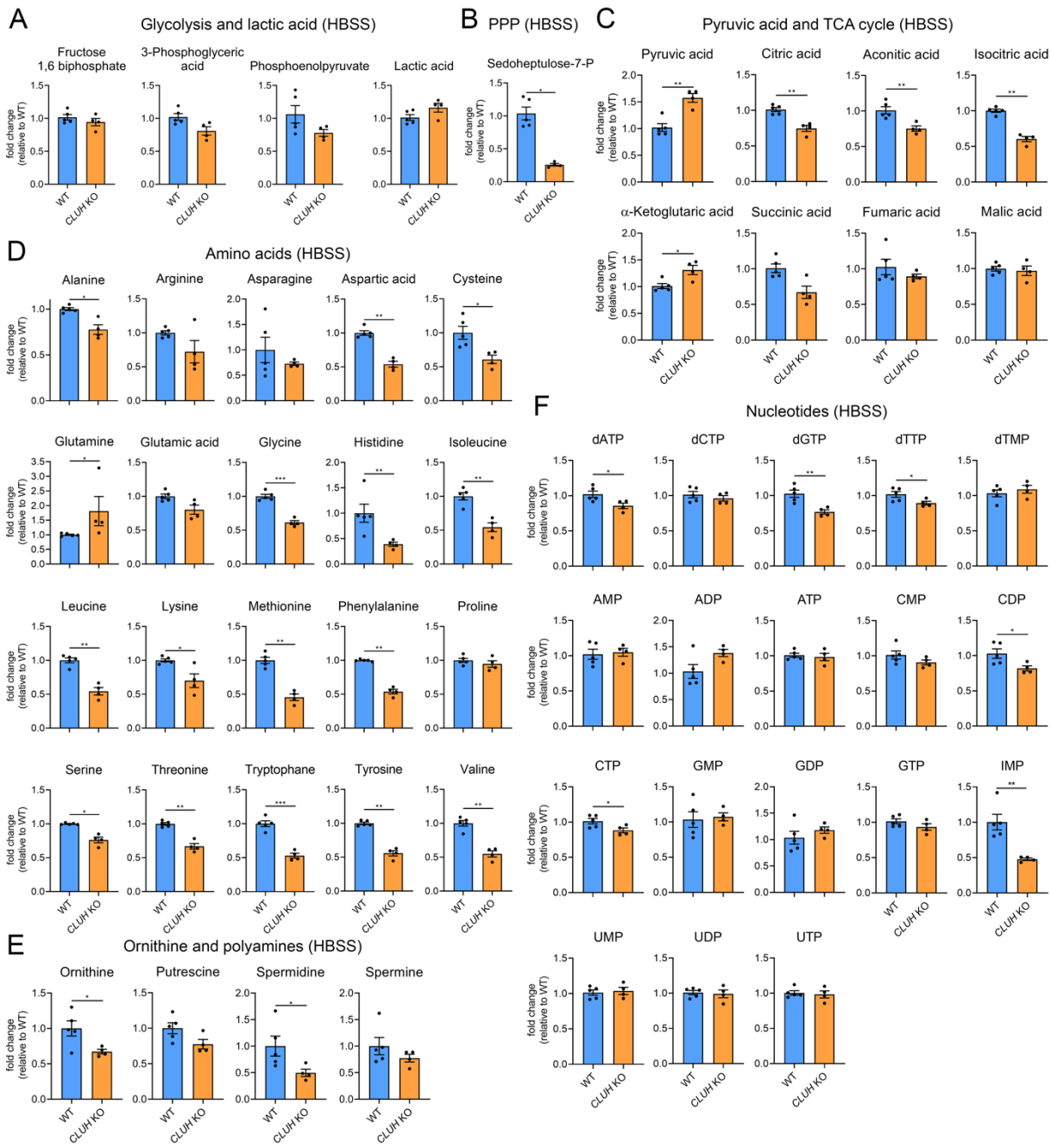

Figure 7. Depletion of CLUH impairs anabolic pathways.

(**A-F**) Targeted metabolomics of WT and *CLUH* KO HeLa cells after 8h HBSS starvation showing glycolytic intermediates and lactic acid (A), sedoheptulose-7-P (B), pyruvic acid and TCA cycle intermediates (C), amino acid levels (D), ornithine and polyamine levels (E) and nucleotide levels (F). Bars show mean ± SEM and dots represent values of individual replicates. Two-tailed unpaired Student`s t-tests on log converted fold changes were performed with P≤0.05: *; P≤0.01: **; P≤0.001: ***.

383 ## CLUH controls cell cycle progression

384 In proliferating cells mitochondrial metabolism is constantly adapted to the specific metabolic
385 needs of the different cell cycle phases. Metabolomic analyses during starvation (a treatment
386 that arrests cell proliferation and blocks entry in G2/M) have revealed opposite signatures in
387 cells lacking CLUH or astrin, indicating a perturbed metabolic rewiring. We therefore
388 hypothesized that the functional significance of the interaction of CLUH with astrin and of their
389 reciprocal regulation is to couple mitochondrial metabolism to cell cycle progression. To
390 investigate this possibility, we synchronized wildtype and *CLUH* KO HeLa cells using a double
391 thymidine block (DTB) followed by release for different time points (Figure 8A). To determine
392 the different phases of cell cycle we stained the cells with the DNA dye PI and analyzed them
393 by flow cytometry. *CLUH* KO cells showed different dynamics in cell cycle progression
394 compared to wildtype cells (significant changes in genotype x time in G0/G1, S and G2/M
395 phases; Figure 8B-D). During all time points, slightly more *CLUH* KO cells were in G0/G1
396 phase and less in S and G2/M (Figure 8B-D). Surprisingly, *CLUH* KO cells cycled faster than
397 control cells, with more cells already in G2/M 3 h after the release and more cells entering the
398 next cell cycle at 8 h after release (Figure 8B-E). Consistently, the dynamics of several cell
399 cycle markers was perturbed in *CLUH* KO cells, including precocious phosphorylation of
400 retinoblastoma (p-RB1-Ser807/811) and accumulation of cyclin D3 (Figure 8F). In addition,
401 the inactivating phosphorylation of CDK1 on Tyr15, which occurs in G2 and allows
402 progression into M, showed a different temporal profile (Figure 8F). During G1 the cells double
403 their mass before progressing to M phase and dividing into two daughter cells. *CLUH* KO cells
404 showed a reduced cell size at all time points during the release, in agreement with the defective
405 growth pathways detected by the metabolomics (Figure 8G). Thus, upon loss of CLUH, HeLa
406 cells escape the growth and energy check-point at the end of G1 and proceed faster through the
407 cell cycle. Our results thus identify CLUH as a novel coordinator of mitochondrial activity with
408 the cell cycle progression (Figure 8-figure supplement 1).

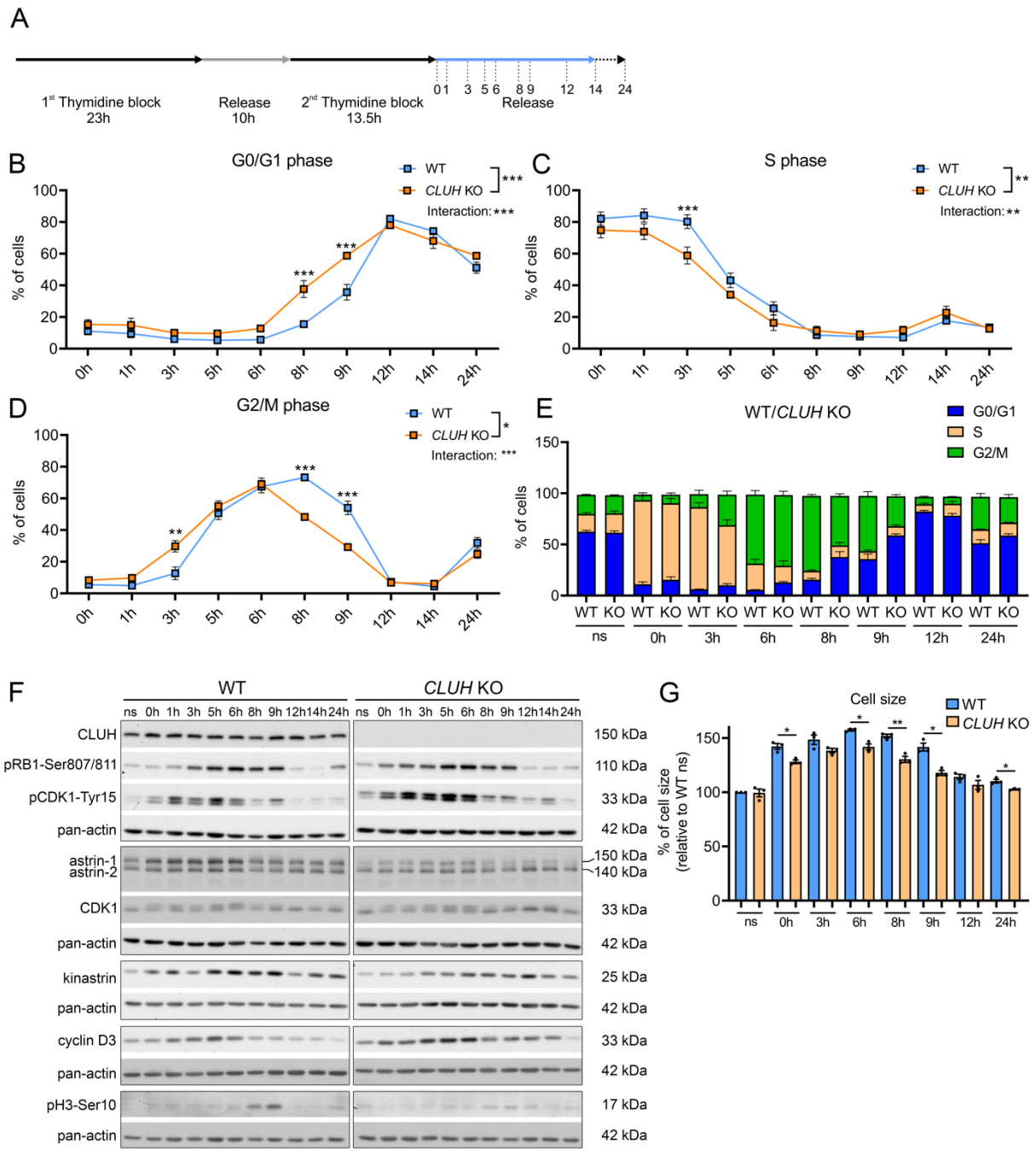

Figure 8. CLUH controls cell cycle progression at the G1/S boundary.

(**A**) DTB synchronization protocol used for cell cycle progression analysis. Cells were collected after release of 2nd thymidine block at indicated time points. (**B-E**) Percentage of WT and *CLUH* KO HeLa cells in G0/G1 (B) in S (C) and G2/M phase (D) and cell cycle distribution analysis (E) after DTB synchronization, collection at indicated time points and PI staining followed by flow cytometric analysis (n=3 independent experiments). For B-D, two-way ANOVA with post hoc Tukey`s multiple comparison tests were performed with P≤0.05: *; P≤0.01: **; P≤0.001: ***. Genotype x time interaction significance is also shown. Graphs and bars show mean ± SEM. (**F**) Western blots of WT and *CLUH* KO HeLa cells collected after

419 DTB synchronization at indicated time points. Pan-actin was used as loading control. (**G**) Cell
420 size analysis of WT and *CLUH* KO HeLa cells of experiments shown in B-E. Bars show mean
421 ± SEM and dots represent values of individual replicates. Two-tailed paired Student`s t-tests
422 were performed with P≤0.05: *; P≤0.01: **.

423

424 DISCUSSION

425 We have uncovered a role of CLUH in integrating mitochondrial metabolism with cell cycle
426 progression. Mechanistically, CLUH controls the synthesis and the stability of astrin-1, the full-
427 length protein product of the *SPAG5* gene. Astrin is a coiled-coil protein, with a well-
428 established role during mitosis to stabilize kinetochore-microtubule interactions and allow
429 correct orientation of chromosomes at the metaphase plate (Manning et al, 2010; Dunsch et al,
430 2011; Kern et al, 2017; Ying et al, 2020). Moreover, additional roles of astrin have been
431 reported in interphase, including mTORC1 inhibition (Thedieck et al, 2013), centriole
432 duplication (Kodani et al, 2015), and the recovery from DNA damage at the G2/M transition
433 (Halim et al, 2013). We show here that the interaction of CLUH with astrin is regulated during
434 the cell cycle, and ensures the matching of the mitochondrial metabolic output with the
435 progression of the cell cycle.
436 *SPAG5* upregulation in several cancers has been associated with poor prognosis (Yuan et al,
437 2014; Abdel-Fatah et al, 2016; Bertucci et al, 2016; Zhou et al, 2018; Li et al, 2019). Human
438 cancer cell lines show the expression of two isoforms of astrin, however the origin of these
439 isoforms has not been investigated up to now. We demonstrate that the two astrin isoforms arise
440 by alternative translation initiation, and are regulated by the presence of an uORF and
441 downstream AUGs with good Kozak sequences. Intriguingly, CLUH interacts only with the
442 full-length astrin-1 protein. The N-terminal region of astrin is an unstructured domain that is
443 dispensable for interaction with kinastrin, DYNLL1, MYCBP and the kinetochore (Kern et al,
444 2017). Recently, the PLK1 kinase has been shown to interact with and phosphorylate the astrin

445 N-terminus, an important step to stabilize the kinetochore-microtubule attachment (Geraghty
446 et al, 2021). Based on our findings, we speculate that N-terminal phosphorylations are
447 responsible for the lack of interaction of CLUH and astrin-1 in prometaphase. Thus, astrin
448 detaches from CLUH during mitosis when it is required for metaphase to anaphase progression.

449 Interestingly, CLUH appears to regulate astrin-1 expression at multiple levels. The *SPAG5*
450 transcript represents an exception to the finding that mRNAs bound by CLUH mainly encode
451 mitochondrial proteins (Gao et al, 2014). We show here that the *SPAG5* mRNA decays faster
452 and that the synthesis of astrin-1 is impaired in absence of CLUH. It is known that during
453 cytokinesis the E3-ubiquitin ligase MID2 ubiquitinates astrin, targeting it for proteosomal
454 degradation (Gholkar et al, 2016). CLUH may be implicated in supporting synthesis of astrin-
455 1 to replenish its levels in G1. Astrin-1 then accumulates during the S and G2 phases of the cell
456 cycle and is stabilized, together with kinastrin, by binding CLUH.

457 The interaction of CLUH with astrin-1 led us first to investigate the possibility of a role of
458 astrin-1 in concert with CLUH in regulating mitochondrial metabolism. Our data do not support
459 this scenario, since depletion of astrin or kinastrin do not recapitulate the prominent
460 mitochondrial defects observed upon CLUH downregulation or knock-out. Upon loss of astrin
461 or kinastrin, mitochondria are normally dispersed in the cytoplasm, show normal morphology
462 and ultrastructure, do not lose mtDNA and efficiently assemble respiratory supercomplexes.
463 *SPAG5* ind-KO cells showed a mild decrease of the levels of mitochondrial proteins encoded
464 by CLUH target mRNAs. Furthermore, starved cells lacking astrin or CLUH display strikingly
465 opposite metabolic profiles. Finally, astrin and kinastrin are not detected in polysomal fractions,
466 in contrast to CLUH.

467 Our data establish an essential role of CLUH in the metabolic rewiring directed by mTORC1
468 signaling. Upon starvation, both *CLUH* KO and *SPAG5* ind-KO cells showed inappropriate

469 mTORC1 activation, in agreement with astrin being a negative regulator of mTORC1
470 (Thedieck et al, 2013). However, the metabolic defects caused by loss of CLUH were
471 discordant with this signaling, with a decrease in the TCA cycle intermediates and in the pool
472 of glycolytic intermediates, some nucleotides, and polyamines. Enzymes of the TCA cycle as
473 well as characteristic anaplerotic enzymes, such as pyruvate carboxylase, proprionyl-CoA
474 carboxylase and other branched amino-acid catabolic enzymes are encoded by *bona fide* CLUH
475 target mRNAs (Gao et al, 2014). These pathways are essential to replenish the TCA cycle
476 intermediates to compensate for their loss upon activation of biosynthetic pathways following
477 mTORC1 signaling. Indeed, a compensatory increase in anaplerotic pathways occurs under
478 conditions of chronic mTORC1 activation (Dutchak et al, 2018). Therefore, CLUH tunes
479 mTORC1 signaling in two independent ways, by regulating the expression of astrin-1 and by
480 ensuring the maintenance of mitochondrial anaplerotic pathways via its RNA-binding function
481 (Figure 8-figure supplement 1). Our data demonstrate another connection between mTORC1
482 signaling and mitochondrial function. mTORC1 positively regulates the translation of
483 mitochondrial proteins involved in oxidative phosphorylation and mitochondrial dynamics
484 (Morita et al, 2013; Morita et al, 2017), while inhibition of mTORC1 activates a lipid signaling
485 cascade that triggers YME1L-mediated intramitochondrial proteolysis to limit mitochondrial
486 biogenesis (MacVicar et al, 2019). Furthermore, mTORC1 hyperactivation is part of the
487 integrated stress response that follows mitochondrial dysfunction (Khan et al, 2017).

488 Proliferating cells must shunt metabolites into mitochondrial pathways that promote cell growth
489 or oxidative respiration and ATP production, depending on the cell cycle phase (DeBerardinis
490 et al, 2008; Salazar-Roa & Malumbres, 2017). In G1 cells double their mass and depend on
491 glycolysis to fuel the TCA cycle and sustain biosynthetic pathways, while in S synthesis of
492 nucleotides is required and glutamine oxidation is prevalent. Interestingly, the TCA cycle
493 intermediates fluctuate during the cell cycle, and it is known that these variations are not

494 transcriptionally regulated (Olsen et al, 2010; Ahn et al, 2017). In mammalian cells, mTORC1
495 activation is important for the transition from G1 to S, an important check point when the energy
496 levels and the growth status of the cell are sensed, and from G2 to M (Cuyàs et al, 2014). We
497 hypothesize that by regulating astrin-1 and stabilizing an RNA regulon involved in the TCA
498 cycle and anaplerotic pathways (Gao et al, 2014), CLUH ensures that the progression of the
499 cell cycle is adjusted with activation of mTORC1 signaling and the mitochondrial metabolic
500 profile (Figure 8-figure supplement 1). Using a post-transcriptional mechanism to coordinate
501 mitochondrial function with cell cycle phases allows a fast and flexible mean to control a broad
502 gene program. Consistently, cells lacking CLUH have cell cycle defects, characterized by a
503 faster cell cycle progression despite failure to properly double the cell mass.

504 Our data not only support a role of CLUH to sustain the mTORC1 signaling cascade, but reveal
505 astrin-1 as a negative regulator of CLUH. Astrin dynamically regulates CLUH subcellular
506 localization: astrin-1 overexpression depletes endogenous CLUH from the cytoplasm and
507 recruits it around the centrosome, while *SPAG5* KO cells show an enrichment of CLUH in
508 structures that contain focal adhesion markers at the plasma membrane. Intriguingly, one study
509 has recently shown that the spatial association of mTORC1 to focal adhesions is not only
510 necessary but also sufficient for the cellular response to growth-promoting signals (Rabanal-
511 Ruiz et al, 2021). Thus, by binding the *SPAG5* mRNA and controlling the stability of astrin-1,
512 CLUH regulates its own subcellular distribution and physiological function. These kinds of
513 feedbacks are commonly operating in metabolic circuits that need to respond to external stimuli,
514 and then recover the original status. It is possible that by sequestering CLUH at the centrosome,
515 astrin-1 puts a break on mTORC1 signaling.

516 More work is needed to characterize the composition and role of the peripheral CLUH
517 structures that we observe upon astrin depletion. Currently, we do not know if these structures
518 contain mRNAs, are translationally active, or recruit mTORC1 components. Moreover, the

519 question arises of the role of CLUH recruitment at the centrosome, which is also strongly
520 supported by the finding of other centrosomal proteins, besides astrin-1, as CLUH molecular
521 partners. Astrin is a component of centriolar satellites in interphase, and it is required for the
522 centrosomal localization of CDK5RAP2, a protein involved in microcephaly, and for proper
523 centriole duplication in S phase (Thein et al, 2007; Kodani et al, 2015), a step which is crucial
524 for cell cycle progression. By recruiting CLUH at the centrosome, astrin may confer a novel
525 signaling role to this organelle, by dynamically relying information on the mitochondrial
526 metabolic status to match it with the progression of the cell cycle. Whether also mRNAs bound
527 to CLUH are recruited to the centrosome is a question to be explored in the future. Finally, our
528 data add to the evidence that astrin plays additional roles outside mitosis. Astrin was also
529 identified in an unbiased screen to be essential for the reentry in mitosis after DNA damage
530 (Halim et al, 2018). This interphase role of astrin should be further explored in view of our
531 findings, as possibly involving dysregulated or enhanced CLUH activity.

532 HeLa cells, as many human cancer cells, overexpress not only astrin-1 but also astrin-2, an
533 isoform of astrin competent to bind all other interactors (kinastrin, DYLNN1 and MYCPB) and
534 the kinetochore (Kern et al, 2017), but not CLUH. We propose that expression of astrin-2
535 endows cancer cells with the ability to proliferate, despite a dysregulated coupling between
536 mitochondrial metabolism and the cell cycle, making CLUH a possible novel therapeutic target
537 in cancers overexpressing *SPAG5*. In conclusions, our findings reveal a novel post-
538 transcriptional mechanism coordinating mitochondrial metabolism and the cell cycle.

539

540 # MATERIAL AND METHODS

541

542 **Cell lines**

543 HeLa WT and *CLUH* KO cells and immortalized WT and *Cluh* KO MEFs were previously
544 described (Gao et al, 2014; Wakim et al, 2017). Doxycycline inducible CRISPR-Cas9 HeLa
545 WT, *SPAG5* and *KNSTRN* KO cells (Kern et al, 2017; McKinley & Cheeseman, 2017) were
546 kindly provided by Iain Cheeseman (Whitehead Institute for Biomedical Research, Cambridge,
547 USA). To produce inducible HEK293T cells stably expressing 3xFLAG-kinastrin, full length
548 N-terminally 3xFLAG tagged human *KNSTRN* ORF was cloned into pTREx-DEST30 vector
549 by serial Gateway recombinations (Invitrogen) according to the manual. Stable transfected
550 HEK293T cells were generated with the Flp-In T-REx 293 cell system (Invitrogen) following
551 the manual. Positive cells were selected with media containing 1.5 mg/mL hygromycin
552 (InvivoGen) and 150 µg/mL blasticidin (InvivoGen) starting 24h after transfection and single
553 colonies were picked to generate a monoclonal cell line.

554

555 **Cell culture**

556 All cells were cultured at 37°C and 5% constant CO_2 supply. All cell culture media and
557 ingredients were purchased from Gibco unless stated otherwise. HeLa cells and MEFs were
558 grown in Dulbecco`s modified eagle medium (DMEM) including 4.5 g/L glucose supplemented
559 with 2 mM L-glutamine, 2% penicillin (10,000 u/mL)/ streptomycin (10,000 µg/mL) and 10%
560 FetalClone III serum (Hyclone, Thermo Fisher Scientific). HEK293T cells were cultured in
561 DMEM including 4.5 g/L glucose supplemented with 2 mM L-glutamine, 1 mM sodium
562 pyruvate, 1% nonessential amino acids, 10% tetracycline free fetal bovine serum (Biochrom
563 AG), 1.5 mg/mL hygromycin and 150 µg/mL blasticidin. To induce overexpression, cells were
564 treated with 1 µg/mL tetracycline (Sigma-Aldrich) for 16h. Doxycycline inducible CRISPR-
565 Cas9 HeLa WT, *SPAG5* and *KNSTRN* KO cells were grown in DMEM containing 4.5g/L

566 glucose supplemented with 2 mM L-glutamine, 2% penicillin (10,000 u/mL)/ streptomycin
567 (10,000 µg/mL) and 10% tetracycline free fetal bovine serum (Sigma-Aldrich). To induce Cas9
568 expression, cells were treated with 1 µg/mL doxycycline (Sigma-Aldrich) for four consecutive
569 days adding fresh doxycycline each day. To obtain stable S*PAG5* and *KNSTRN* KO cell lines,
570 induced cells underwent monoclonal selection after serial dilutions.
571
572 **Metabolic labeling**
573 For metabolic labelling of newly synthesized astrin, cells were primed in metabolic labeling
574 medium [DMEM containing 4.5 g/L glucose without L-methionine and L-cystine (#21013024,
575 Gibco) including 10% dialysed serum, 2% penicillin (10,000 u/mL)/ streptomycin (10,000
576 µg/mL), 2 mM L-glutamine, 1 mM sodium pyruvate and 1% non-essential amino acids] for 30
577 min followed by incubation with metabolic labeling medium including ^{35}S-methionine (50 µCi
578 per 10 cm plate) for indicated time points.
579
580 **SILAC labeling**
581 Cells were cultured in DMEM medium without glutamine, arginine and lysine (Silantes, #
582 280001200), supplemented with 2 mM L-glutamine, 2% penicillin/ streptomycin, dialyzed FCS
583 (Thermofisher, # 26400044), 28 µg/mL L-arginine-HCl (Arg0 or Arg10) (Silantes, #
584 201604102) and 73 µg/mL L-lysine-2HCl (Lys0 or Lys8) (Silantes, # 211604102) for three
585 passages before collecting for IP.
586
587 **CHX chase and galactose treatment**
588 To assess protein stability, cells were treated with 0.1 mg/mL CHX (Sigma-Aldrich) with or
589 without 20 µM MG132 (Sigma-Aldrich) for indicated time points. Cells were grown when
590 indicated in galactose media [DMEM, no glucose (#11966-025, Gibco) supplemented with 10
591 mM galactose (Sigma-Aldrich), 2 mM L-glutamine, 1 mM sodium pyruvate, 2% penicillin

592 (10,000 u/mL)/ streptomycin (10,000 µg/mL) and 10% dialyzed fetal bovine serum (Gibco)]
593 for 16 h before experiments were performed.
594
595 **Cloning and mutagenesis of SPAG5 constructs**
596 The underlying sequence of human *SPAG5* used in this study can be found under the accession
597 number NM_006461.3 on the NCBI database. Human full length *SPAG5* ORF (ATG1-SPAG5)
598 or excluding the first 453 nucleotides (Δ151-SPAG5) were cloned into p3xFLAG-CMV-14
599 (Sigma-Aldrich) using NotI or NotI/ClaI restriction sites, respectively. To obtain a construct
600 including the 5´ UTR (5UTR-SPAG5), the 5´ UTR of *SPAG5* was cloned into Δ151-SPAG5-
601 FLAG using HindIII restriction site. To mutagenize ATGs to GGG, DpnI site directed
602 mutagenesis was employed. Mutagenized base pair positions and construct names are indicated
603 in Figure 1C and S1A.
604
605 **Cell transfection**
606 Cells were transfected with Lipofectamine 2000 (Invitrogen) in a plasmid to transfection
607 reagent ratio of 1:5 according to the manual. After 24 h of overexpression, cells were harvested
608 by scraping and pelleting for lysis or fixed with respective reagent for immunofluorescence.
609 RNA interference of *CLUH* was done as described before (Gao et al, 2014). Briefly, HeLa cells
610 were transfected with 100 nM of siRNA against human *CLUH* or control siRNA using
611 Lipofectamine 2000 according to the instructions of the manual and experiments were
612 performed after 72h of downregulation.
613
614 **Polysome profiling**
615 Cells were grown in 15 cm dishes to 70-80% confluency and treated for 15 min with fresh
616 media supplied with 100 µg/mL CHX (Sigma Aldrich), followed by crosslinking with 1 mM
617 dithiobis (succinimidyl propionate) (DSP) in PBS for 30 min at RT. prior to polysome profiling

618 followed by immunoblotting. Cells were washed with PBS and quenched in 20 mM Tris-HCl,
619 pH 7.4, 5 mM L-cysteine for 10 min. Cells were then washed twice with ice cold PBS
620 containing 100 µg/mL CHX and scraped in 1.5 mL ice cold PBS including CHX and collected
621 in a 2 mL tube. Cells were immediately centrifuged at 21,000 x g for 10 sec at 4°C and
622 supernatant was discarded. Cells were lysed for 30 min on ice in buffer comprised of 20 mM
623 Tris-HCl, pH 7.4, 30 mM KCl, 15 mM MgCl2, 0.5% Triton X-100 (vol/vol), 2 mM DTT, 1
624 mg/mL heparin, 100 µg/mL CHX, 0.16 U/mL RNase inhibitor (RNasin Plus; Promega), and
625 1× EDTA-free protease cocktail (Roche). Cell debris were then removed with 5 min
626 centrifugation at 14 000 x g at 4°C and protein concentration was measured with the standard
627 Bradford assay. Cell lysate was then applied on a continuous 7-47% sucrose gradient (mol
628 weight/volume) in ultra clear tubes (Beckman & Coulter, #331372) and centrifuged at 97,658
629 x g for 3 h at 4°C using a SW41Ti rotor (Beckman & Coulter, # 331362). The polysome
630 fractions were collected using the Foxy R1 Fraction Collector and immediately snap frozen
631 with liquid nitrogen and stored at -80 °C. The polysome profile was detected with the UA-6
632 detector (Teledyne ISCO) during the collection of each polysome fraction.
633
634 **Synchronization of cells**
635 Cells were synchronized by double thymidine block (DTB) using an adapted protocol (Dai et
636 al, 2018). Briefly, cells were plated in desired amount and treated the next day with 2 mM
637 thymidine (Sigma-Aldrich) for 23 h, afterwards cells were released in standard media without
638 thymidine for 10h and second thymidine block (2 mM thymidine) was performed for 13.5 h.
639 Next day, cells were released and collected at indicated time points depending on the
640 experiment (Figure 3-figure supplement 1A, 8A). To enrich cells in PM phase, cells were
641 treated with 100 ng/µl nocodazole (Sigma-Aldrich) after 3 h of release and collected after 12
642 additional hours. To block cells in G0/G1, cells were starved in media without serum for 16h.
643

644 **Immunoprecipitations**

645 For IP cells were collected and lysed in an appropriate volume of IP buffer [50 mM Tris-HCl,
646 pH7.4; 50 mM KCl; 0.1% Triton X-100 supplemented freshly with protease inhibitor cocktail
647 (Sigma-Aldrich)] for 30 min on ice after passing 3x through syringe (30G x 1/2", B. Braun
648 Sterican). For SILAC samples, the lysate was incubated with 25 U benzonase HC nuclease
649 (Sigma-Aldrich) at 37 °C for 30 min before IP. Afterwards, lysates were cleared by
650 centrifugation at 20,000 x g for 30 min and protein amount was determined by standard
651 Bradford assay (Biorad). For each reaction, 300-500 µg of protein were diluted in 250 µl IP
652 buffer and incubated for 3h in head-to-toe agitation at 4°C with 0.5 µg of the specific antibody:
653 rabbit polyclonal rabbit anti-CLUH [#NB100-93305 (1) and #NB100-93306 (2) from Novus
654 Biologicals]; rabbit polyclonal anti-kinastrin (#SAB1103031 from Sigma-Aldrich); rabbit
655 polyclonal anti-astrin (#14726-1-AP from ProteinTech; #NB100-74638 from Novus
656 Biologicals). As control antibodies, we used rabbit polyclonal anti-AFG3L1 (Koppen et al,
657 2007) (Figure 1A, B and Figure S1C) and rabbit polyclonal anti-FLAG (#F7425 from Sigma-
658 Aldrich) (Figure 3, Figure S1B, D). 20 µl of prewashed magnetic Dynabeads Protein G
659 (Invitrogen) were added per reaction and incubated for 1 h in head-to-toe agitation at 4°C.
660 Afterwards, beads were washed five times with IP buffer. To elute kinastrin, beads were
661 incubated in 100 mM glycine, pH 2.3 for 20 min at 4°C. In the other cases, proteins were eluted
662 in 30 µl 3x Laemmli buffer (20 mM Tris-HCl, pH 6.8, 2% SDS, 5% β-mercaptoethanol, 2.5%
663 glycerol and 2.5% bromophenol blue) by vortexing for 1 min and boiling at 95°C for 5 min.
664 Samples were stored at -20°C or run immediately on SDS-PAGE.

665

666 **Sample preparation for mass spectrometry**

667 For IP of CLUH followed by mass spectrometry of WT cells enriched in G2, experiments were
668 carried out as described before using 400 µg lysate as input and elution was done with 30 µl
669 SP3 lysis buffer (5% SDS in 1x PBS) by vortexing for 1 min and boiling at 95°C for 5 min.

670 Afterwards, proteins were reduced with 5 mM dithiothreitol for 30 min at 55°C and alkylated
671 with 40 mM chloroacetamide at RT for 30 min in the dark. Next, samples were centrifuged at
672 20,000 x g for 10 min and supernatant was transferred to new tube and stored at -20°C before
673 mass spectrometry was performed. For SILAC labelled samples, beads were resuspended in 50
674 µl of elution buffer 1 (2M urea, 50 mM triethylammoniumbicarbonate, 1 mM DTT, 5 ng/µl
675 trypsin) and incubated at RT for 30 min while shaking. Beads were centrifuged and supernatant
676 transferred to a new tube. Beads were washed twice with elution buffer 2 (2M urea, 50 mM
677 triethylammoniumbicarbonate, 5 mM chloroacetamide) and centrifuged. The eluates were
678 combined. Next, proteins were digested with lysyl endopeptidase (Wako Pure Chemical
679 Industries) and trypsin (Sigma-Aldrich) with an enzyme:substrate ratio of 1:75 at 37 °C for 16
680 h. Next day, samples were acidified with formic acid to stop enzymatic digestion, purified with
681 and loaded on StageTips as described before (Rappsilber et al, 2007).
682 HeLa WT, *SPAG5* and *KNSTRN* ind-KO cells were collected by scraping, pelleted and
683 resuspended in appropriate amount of lysis buffer [50 mM Tris-HCl, pH 7.4; 150 mM NaCl; 1
684 mM EDTA, pH8; 1% IGEPAL CA-630; 0.25% sodium deoxycholate freshly supplemented
685 with protease inhibitor cocktail (Sigma-Aldrich)]. Lysates were passed 3x through syringe (30G
686 x 1/2", B. Braun Sterican) and incubated on ice for 30 min. After centrifugation for 30 min at
687 20,000 x g at 4°C, protein amounts were determined using standard Bradford assay (Biorad)
688 and 30 µg of protein lysate were precipitated with acetone. Briefly, 4x volume of ice-cold
689 acetone were added to lysates, incubated for 15 min at -80°C followed by 90 min incubation at
690 -20°C and centrifugation for 15 min at 16,000 x g. Pellets were washed in ice-cold acetone, air-
691 dried and resuspended in 50 µl of 8 M urea in 50 mM triethylammoniumbicarbonate including
692 protease inhibitor cocktail (Roche). Afterwards proteins were reduced with 5 mM dithiothreitol
693 for 1h at 25°C and alkylated with 40 mM chloroacetamide for 30 min in the dark. Next, proteins
694 were digested with lysyl endopeptidase (Wako Pure Chemical Industries) with an
695 enzyme:substrate ratio of 1:75 at 25°C for 4h. Samples were diluted with 50 mM

696 triethylammoniumbicarbonate to reach a final urea concentration of 2 M. Then proteins were
697 digested with trypsin (Sigma-Aldrich) with an enzyme:substrate ratio of 1:75 and incubation at
698 25°C for 16 h. Next day, samples were acidified with formic acid to stop enzymatic digestion,
699 purified with and loaded on StageTips as described before (Rappsilber et al, 2007). Samples
700 were stored in dried StageTips at 4°C until mass spectrometry was performed.
701
702 **Mass spectrometry of CLUH IP after SILAC**
703 SILAC labelled samples were analyzed on a Q Exactive Plus Orbitrap (Thermo Scientific) mass
704 spectrometer that was coupled to an EASY nLC (Thermo Scientific). Peptides were loaded with
705 solvent A (0.1% formic acid in water) onto an in-house packed analytical column (50 cm x 75
706 µm I.D., filled with 2.7 µm Poroshell EC120 C18, Agilent). Peptides were chromatographically
707 separated at a constant flow rate of 250 nL/min using the following gradient: 7-23% solvent B
708 (0.1% formic acid in 80 % acetonitrile) within 35.0 min, 23-32% solvent B within 5.0 min, 32-
709 85% solvent B within 5.0 min, followed by washing and column equilibration. The mass
710 spectrometer was operated in data-dependent acquisition mode. The MS1 survey scan was
711 acquired from 300-1750 m/z at a resolution of 70,000. The top 10 most abundant peptides were
712 isolated within a 1.8 Th window and subjected to HCD fragmentation at a normalized collision
713 energy of 27%. The AGC target was set to 5e5 charges, allowing a maximum injection time of
714 108 ms. Product ions were detected in the Orbitrap at a resolution of 35,000. Precursors were
715 dynamically excluded for 20.0 s. All mass spectrometric raw data were processed with
716 Maxquant (version 1.5.3.8) using default parameters. Briefly, MS2 spectra were searched
717 against the Uniprot HUMANc_UP000005640.fasta (downloaded at: 26.08.2020) database,
718 including a list of common contaminants. False discovery rates on protein and PSM level were
719 estimated by the target-decoy approach to 1% (Protein FDR) and 1% (PSM FDR) respectively.
720 The minimal peptide length was set to 7 amino acids and carbamidomethylation at cysteine
721 residues was considered as a fixed modification. Oxidation (M) and Acetyl (Protein N-term)

722 were included as variable modifications. SILAC/dimethyl labeling quantification was used, and
723 the re-quantify option was enabled.
724
725 **Mass spectrometry of CLUH IP in synchronized cells**
726 Immunoprecipitated proteins from cells synchronized in G2 were analyzed on a Q-Exactive
727 Plus (Thermo Scientific) mass spectrometer that was coupled to an EASY nLC 1200 UPLC
728 (Thermo Scientific). Peptides were loaded with solvent A (0.1% formic acid in water) onto an
729 in-house packed analytical column (50 cm × 75 µm I.D., filled with 2.7 µm Poroshell EC120
730 C18, Agilent). Peptides were chromatographically separated at a constant flow rate of 250
731 nL/min using the following gradient: 3-5% solvent B (0.1% formic acid in 80 % acetonitrile)
732 within 1 min, 5% - 30% solvent B (0.1% formic acid in 80 % acetonitrile) within 40 min, 30%
733 -50% solvent B 8 min and 40% to 95% solvent B within 1 min, followed by washing with 95%
734 solvent B for 10 min. The mass spectrometer was operated in data-dependent acquisition mode.
735 The MS1 survey scan was acquired from 300 to 1750 m/z at a resolution of 70,000. The top 10
736 most abundant peptides were isolated within a 1.8 Th window and subjected to HCD
737 fragmentation at a normalized collision energy of 27%. The AGC target was set to 5e5 charges,
738 allowing a maximum injection time of 110 ms. Product ions were detected in the Orbitrap at a
739 resolution of 35,000. Precursors were dynamically excluded for 10 s. All mass spectrometric
740 raw data were processed with MaxQuant version 1.5.3.8 (Tyanova et al, 2016b) using default
741 parameters. Briefly, MS2 spectra were searched against a canonical Uniprot human fasta
742 database, which was modified by replacing the default entry for SPAG5 (Q96R06) by two
743 separate entries representing (i) the N-terminal 125 amino acids and (ii) the C-terminal
744 sequence from position 126 on. The MaxQuant default list was used to filter for common
745 contaminants. False discovery rates on protein and PSM level were estimated by the target-
746 decoy approach to 1% (Protein FDR) and 1% (PSM FDR) respectively. The minimal peptide
747 length was set to 7 amino acids and carbamidomethylation at cysteine residues was considered

748 as a fixed modification. Oxidation (M) and Acetyl (Protein N-term) were included as variable
749 modifications. The match-between runs option was restricted to replicates of the same
750 condition. LFQ quantification was used with default settings. LFQ intensities were loaded into
751 in Perseus version 1.6.1.1 (Tyanova et al, 2016a). Decoys and potential contaminants were
752 removed and the dataset was filtered for at least 4 out of 4 values in at least one condition.
753 Remaining missing values were imputed with random values from the left end of the intensity
754 distribution using Perseus defaults. Two sample Student's T-test were calculated using
755 permutation-based FDR estimation.
756
757 **Mass spectrometry of *SPAG5* and *KNSTRN* ind-KO cells**
758 For proteomics of HeLa WT ind, *SPAG5* and *KNSTRN* ind-KO cells, peptide digests were
759 analyzed on a Q Exactive plus Orbitrap (Thermo Scientific) mass spectrometer that was coupled
760 to an EASY nLC (Thermo Scientific). Samples were loaded onto an in-house packed analytical
761 column (50 cm x 75 µm I.D., filled with 2.7 µm Poroshell EC120 C18, Agilent). Peptides were
762 separated at a flow rate of 250 nL/min and the following gradient: 3-5% solvent B (0.1% formic
763 acid in 80 % acetonitrile) within 1.0 min, 5-30% solvent B within 91.0 min, 30-50% solvent B
764 within 17.0 min, 50-95% solvent B within 1.0 min, followed by washing with 95 % solvent B
765 for 10 min. DDA runs for spectrum library generation were acquired from distinct pools of the
766 sample groups and Hek293 cell digests fractionated high pH HPLC. MS1 survey scan were
767 acquired at a resolution of 70,000. The top 10 most abundant peptides were isolated within a
768 2.0 Th window and subjected to HCD fragmentation with normalized collision energy of 27%.
769 The AGC target was set to 5e5 charges, allowing a maximum injection time of 105 ms. Product
770 ions were detected in the orbitrap at a resolution of 35,000. Precursors were dynamically
771 excluded for 20.0 s. Sample runs were acquired in data-independent mode using 10 variable
772 windows covering the mass range from m/z 450 to m/z 1200. MS1 scans were acquired at
773 140,000 resolution, maximum IT restricted to 120 ms and an AGC target set to 5e6 charges.

774 The settings for MS2 scans were 17,500 resolution, maximum IT restricted to 60 ms and AGC
775 target set to 5e6 charges. The default charge state for the MS2 was set to 4. Stepped normalized
776 collision energy was set to 23.5, 26 and 28.5. All spectra were acquired in profile mode. A
777 hybrid spectrum library was generated in Spectronaut 13 (Bruderer et al, 2015) using DDA
778 library runs, DIA sample runs and a canonical human sequence file (SwissProt, 20416 entries)
779 downloaded from Uniprot. Spectronaut default settings were used for the analysis of the DIA
780 runs. Protein identifications were filtered for q-values below 0.01 and normalized intensities
781 were exported for subsequent statistical analysis in Perseus 1.6.1.1 (Tyanova et al, 2016b).
782 Intensities were transformed to log2 values and the dataset was filtered for at least 4 out of 4
783 values in at least one condition. Remaining missing values were imputed with random values
784 from the left end of the intensity distribution (with 0.3 sd, downshift 2 sd). Two sample
785 Student´s T-tests were calculated using permutation based FDR estimation.
786
787 **Proteomics visualization and pathway analysis**
788 Enriched proteins of IP experiment or proteomics results were visualized as volcano plots using
789 Instant Clue software (Nolte et al, 2018) and pathway analysis was carried out using the
790 EnrichR webtool with a cut off of $q \leq 0.05$ and log2 fold change ≥ 3 for the IP and a cut off of
791 $q \leq 0.15$ and $p \leq 0.05$ for the proteomics analysis (Chen et al, 2013; Kuleshov et al, 2016; Xie et
792 al, 2021).
793
794 **Isolation of mitochondria**
795 Cells were collected from confluent 15 cm plates with trypsinization, washed twice with PBS,
796 and resuspended in an ice-cold mitochondria isolation buffer containing 20 mM HEPES, pH
797 7.6; 220 mM mannitol; 70 mM sucrose; 1 mM EDTA; 0.2% fatty acid-free bovine serum
798 albumin (BSA). After 20 min of incubation on ice, cells were homogenized using the rotational
799 engine homogenizer (Potter S, Sartorius; 30 strokes, 1200 rpm) followed by centrifugation at

800 850 × g. Next, mitochondria were pelleted at 8500 × g for 10 min at 4 °C, washed with BSA-
801 free buffer, and protein concentration was determined with Bradford reagent (Sigma-Aldrich).
802 For further analysis, mitochondria were subjected to blue native polyacrylamide gel
803 electrophoresis (BN-PAGE) followed by western blotting or determination of the in-
804 gel activity of respiratory complexes
805
806 **Analysis of mitochondrial respiratory complexes with BN-PAGE**
807 20 mg of mitochondria were lysed with digitonin (Calbiochem; 6.6 g/g protein) for 15 min on
808 ice with occasional vortexing and cleared from insoluble material for 20 min at 20,000 × g at 4
809 °C. Lysates were combined with Coomassie G-250 (0.25% final concentration). Mitochondrial
810 respiratory supercomplexes were resolved with BN-PAGE using the 4–16% NativePAGE
811 Novex Bis-Tris Mini Gels (Invitrogen) in a Bis-Tris/Tricine buffering system with cathode
812 buffer initially supplemented with 0.02% G-250 followed by the 0.002% G-250. For complex
813 I in-gel activity, gels were incubated at RT in a buffer containing 0.01 mg/mL NADH and 2.5
814 mg/mL nitrotetrazolium blue in 5 mM Tris-HCl, pH 7.4.

815 **Cell lysis and western blot**
816 Cell pellets were lysed in appropriate amount of lysis buffer [50 mM Tris-HCl, pH 7.4; 150
817 mM NaCl; 1 mM EDTA, pH8; 1% IGEPAL CA-630; 0.25% sodium deoxycholate freshly
818 supplemented with protease inhibitor cocktail (Sigma-Aldrich)] and protein amounts were
819 determined by standard Bradford assay (Biorad). Desired protein amounts were mixed with
820 appropriate volume of 3x loading buffer (20 mM Tris-HCl, pH6.8; 2% SDS; 5% β-
821 mercaptoethanol; 2.5% glycerol and 2.5% bromophenol blue), boiled for 5 min at 95°C and
822 loaded on SDS polyacrylamide gels. Proteins were separated by SDS PAGE and blotted on
823 polyvinylidene fluoride (PVDF) membranes using wet transfer. After BN-PAGE, separated
824 mitochondrial complexes were transferred on PVDF membranes using the wet transfer sodium

825 lauryl sulfate (SDS)-free and methanol-free system. The following primary antibodies were
826 used for western blotting: rabbit polyclonal anti-CLUH antibodies [detecting human CLUH;
827 #NB100-93305 (1), #NB100-93306 (2)], rabbit polyclonal anti-RPS6 (#NB100-1595), rabbit
828 polyclonal anti-RPL7 (#NB100-2269) antibodies from Novus Biologicals; rabbit polyclonal
829 anti-astrin (#14726-1-AP) antibody from ProteinTech; rabbit polyclonal anti-FLAG (#F7425)
830 and mouse monoclonal anti-FLAG (#F3165) antibodies from Sigma-Aldrich; mouse
831 monoclonal pan-actin (#MAB1501) and anti-GAPDH (#MAB374) antibodies from EMD
832 Millipore; rabbit polyclonal anti-CLUH antibody (detecting murine CLUH;
833 #ARP70642_P050) from Aviva; rabbit polyclonal anti-kinastrin (#ab122769) and rabbit
834 polyclonal pH3-Ser10 (#ab5176) antibodies from Abcam; mouse monoclonal anti-SDHA
835 (#459200), anti-NDUFA9 (#459100) and anti-UQCRC1 (#459140) from Molecular probes;
836 rabbit polyclonal pRB1-Ser807/811 (#9308), rabbit monoclonal pCDK1-Tyr15 (#4539), mouse
837 monoclonal anti-cyclin D3 (#2936) and rabbit polyclonal pRPS6-Ser235/236 (#2211)
838 antibodies from Cell Signaling and mouse monoclonal anti-CDK1 (#sc-54) antibody from
839 Santa Cruz Biotechnologies.
840
841 **Sample collection to measure anionic metabolites, amino acids and polyamines**
842 WT, *SPAG5* and *KNSTRN* ind-KO cells were induced as described before and 1,000,000 cells
843 were plated in 6 well plates the day before the extraction. Next day, the cells were either
844 collected immediately (basal condition) or starved for 8h in HBSS media (#14025092, Gibco)
845 in absence of doxycycline. Cells were washed twice with buffer containing 75 mM ammonium
846 carbonate (pH7.4) and metabolites were extracted with cold (-20°C) extraction solvent
847 (40:40:20 acetonitrile:methanol:water) and incubation for 10 min at -20°C. Supernatant was
848 collected and extraction was repeated. Afterwards, cells were scraped on ice and combined with
849 the supernatant of the previous step. Samples were immediately dried in a speed vac
850 concentrator and dried pellets were kept at -80°C until mass spectrometry was performed.

851

852 **Anion-Exchange Chromatography Mass Spectrometry (AEX-MS) for the analysis of**
853 **anionic metabolites**

854 Extracted metabolites were re-suspended in 150 µl of Optima LC/MS grade water (Thermo
855 Fisher Scientific), of which 100 µl were transferred to polypropylene autosampler vials
856 (Chromatography Accessories Trott, Germany) before AEX MS analysis. The samples were
857 analysed using a Dionex ionchromatography system (Integrion, Thermo Fisher Scientific) as
858 described previously (Schwaiger et al, 2017). In brief, 5 µL of polar metabolite extract were
859 injected in push partial mode using an overfill factor of 3, onto a Dionex IonPac AS11-HC
860 column (2 mm × 250 mm, 4 µm particle size, Thermo Fisher Scientific) equipped with a Dionex
861 IonPac AG11-HC guard column (2 mm × 50 mm, 4 µm, Thermo Fisher Scientific). The column
862 temperature was held at 30°C, while the auto sampler was set to 6°C. A potassium hydroxide
863 gradient was generated using a potassium hydroxide cartridge (Eluent Generator, Thermo
864 Scientific), which was supplied with deionized water. The metabolite separation was carried at
865 a flow rate of 380 µL/min, applying the following gradient conditions: 0-3 min, 10 mM KOH;
866 3-12 min, 10-50 mM KOH; 12-19 min, 50-100 mM KOH, 19-21 min, 100 mM KOH, 21-22
867 min, 100-10 mM KOH. The column was re-equilibrated at 10 mM for 8 min. For the analysis
868 of metabolic pool sizes the eluting compounds were detected in negative ion mode $[M-H]^-$ using
869 multiple reaction monitoring (MRM) mode with the following settings: Capillary voltage 2.7
870 kV, desolvation temperature 550°C, desolvation gas flow 800 l/h, collision cell gas flow 0.15
871 mL/min. The detailed quantitative and qualitative transitions and electronic settings for the
872 analyzed metabolites are summarized in Supplementary Table 4. The MS data analysis was
873 performed using the TargetLynx Software (Version 4.1, Waters). For data analysis the area of
874 the quantitative transition of each compound was extracted and integrated using a retention time
875 (RT) tolerance of <0.1 min as compared to the independently measured reference compounds.
876 Areas of the cellular pool sizes were normalized to the internal standards (citric acid D4), which

877 were added to the extraction buffer, followed by a normalization to the protein content of the
878 analyzed sample. One sample of *CLUH* KO and one of *SPAG5* ind-KO cells upon HBSS
879 starvation has been classified as outlier and removed from analysis. Samples were classified as
880 outliers due to PCA plot and tremendous drift of measured values from other samples.
881

882 **LC-MS analysis of cellular pool sizes of amino acids and polyamines**

883 For amino acid analysis, the benzoylchlorid derivatization method (Wong et al, 2016) was used.
884 In brief, 20 µl of the polar phase of each sample, were mixed with 10 µl of 100 mM sodium
885 carbonate (Sigma-Aldrich) followed by the addition of 10 µl 2% benzoylchloride (Sigma-
886 Aldrich) in acetonitrile (VWR). Samples were analyzed using an Acquity iClass UPLC
887 (Waters) connected to a Q-Exactive HF (Thermo Fisher Scientific). For analysis, 1 µl of the
888 derivatized sample was injected onto a 100 x 1.0 mm HSS T3 column, packed with 1.8 µm
889 particles (Waters). The flow rate was 100 µL/min and the buffer system consisted of buffer A
890 (10 mM ammonium formate, 0.15% formic acid in water) and buffer B (acetonitrile). The
891 gradient was: 0% B at 0 min; 0-15% B 0-0.1 min; 15-17% B 0.1-0.5 min; 17-55% B 0.5-14
892 min, 55-70% B 14-14.5 min; 70-100% B 14.5-18 min; 100% B 18-19 min; 100-0% B 19-19.1
893 min, 19.1-28 min 0% B. The mass spectrometer was operating in positive ionization mode
894 monitoring and the mass range was set to m/z 50-750. The heated ESI source settings of the
895 mass spectrometer were: Spray voltage 3.5kV, capillary temperature 275°C, sheath gas flow 40
896 AU and aux gas flow 20 AU at a temperature of 300°C. The S-lens was set to 60 AU. Data
897 analysis was performed using the TraceFinder software (Version 4.1, Thermo Fisher
898 Scientific). Identity of each compound was validated by authentic reference compounds, which
899 were injected and analyzed independently. Extracted ion chromatograms (XIC) were extracted
900 as $[M + H]^+$ ions with a mass accuracy (<5 ppm). Areas of the cellular pool sizes of the analyzed
901 amines were normalized to their corresponding $^{13}C^{15}N$ internal standard or, if no corresponding
902 $^{13}C^{15}N$ compound was present, they were normalized to the $^{13}C^{15}N$ leucine. Following the

903 normalization to the internal standard the values were normalized to the protein content of the
904 analyzed sample.
905
906 **Measurement of RNA stability**
907 To measure mRNA stability, Click-iT Nascent RNA Capture Kit (Invitrogen) was used as
908 described before (Schatton et al., 2017). Briefly, 500,000 cells were seeded on 3.5 cm dishes.
909 The following day, endogenous RNA was labeled with 0.2 mM 5-ethynyl uridine (EU) for 24h
910 and collected either immediately (0h time point) or after 8h incubation with media w/o EU with
911 Trizol reagent (Invitrogen). Total RNA was isolated according to the instructions of the Trizol
912 reagent manual and 3 µg RNA were biotinylated with biotin-azide using Click-iT chemistry
913 reaction. Afterwards, RNA was precipitated with glycogen, 7.5 M ammonium acetate and
914 100% ice cold ethanol for 16h and centrifugation at 13,000 x g for 20 min at 4°C. RNA was
915 washed twice with 70% ethanol, air-dried and resuspended in distilled H2O. 1.5 µg RNA were
916 incubated with prewashed Dynabeads MyOne Streptavidin T1 beads (Invitrogen) for 30 min in
917 presence of RNaseOUT (Invitrogen). Afterwards beads were washed several times and RNA
918 bound on beads was retrotranscribed with SuperScript VILO cDNA synthesis kit (Invitrogen)
919 according to the manual. cDNA was stored at -20°C until qRT-PCR was performed. mRNA
920 half-lives were calculated as described before (Schatton et al, 2017).
921
922 **RNA isolation, cDNA synthesis, DNA isolation and quantitative real-time PCR**
923 RNA was isolated with Trizol reagent (Invitrogen) according to the manual. 2 µg of total RNA
924 were retro-transcribed using the SuperScript First-Strand Synthesis System (Invitrogen) with
925 random hexamer primers according to the instructions of the manual. To isolate genomic DNA,
926 cells were lysed with digestion buffer [100 mM NaCl; 10 mM Tris-HCl, pH8; 25 mM EDTA,
927 pH8; 0.5% SDS supplemented freshly with 0.1 mg/mL proteinase K (Roche)] at 55°C for 16h.
928 DNA was isolated with standard phenol/chloroform purification followed by ethanol

929 precipitation. For mtDNA quantification, 20 ng genomic DNA were used per reaction. SYBR
930 green master mix (Applied Biosystems) was used for quantitative real-time PCR using either
931 StepOne Plus Real-Time PCR system or Quant Studio 12K Flex Real-Time PCR Sytem
932 thermocycler (Applied Biosystems). For each reaction technical duplicates and at least three
933 biological replicates per experiment were performed. *GAPDH* or *RPL13* were used for
934 normalization and fold enrichment was calculated with the formula: $2^{(-\Delta\Delta Ct)}$. The following
935 primers were used for amplification: *SPAG5* forward: 5'-
936 CATCTCACAGTGGGATAACTAATAAAC-3'; *SPAG5* reverse: 5'-
937 CAGGGATAGGTGAAGCAAGGATA-3'; *GAPDH* forward: 5'-
938 AATCCCATCACCATCTTCCA-3'; *GAPDH* reverse: 5'-TGGACTCCACGACGTACTCA-3';
939 *RPL13* forward: 5'-CGGACCGTGCGAGGTAT-3'; *RPL13* reverse: 5'-
940 CACCATCCGCTTTTTCTTGTC-3'; *MT-TL1* forward: 5'-CACCCAAGAACAGGGTTTGT-
941 3'; *MT-TL1* reverse: 5'-TGGCCATGGGTATGTTGTTA-3'; *B2M* forward: 5'-
942 TGCTGTCTCCATGTTTGATGTATCT-3'; *B2M* reverse: 5'-
943 TCTCTGCTCCCCACCTCTAAGT-3'.
944
945 **Immunofluorescence and transmission electron microscopy**
946 Cells were seeded in an appropriate amount on coverslips the day before. Next day, cells were
947 washed twice with 1x PBS and fixed for 15 min either with 4% PFA/PBS (pH7.4) or with ice-
948 cold 100% methanol at RT or -20°C, respectively, depending on the primary antibody and as
949 indicated in the figure legends. Afterwards, cells were permeabilized with 0.2% Triton X-100
950 in 1x PBS for 10 min and blocked in 10% pig or goat serum for 10 min. Then coverslips were
951 stained with primary antibodies diluted in 1% pig or goat serum in 1x PBS for 2h at RT or for
952 16h at 4°C. The following primary antibodies were used: rabbit polyclonal anti-CLUH antibody
953 (1:1000, #NB100-93306, Novus Biologicals), mouse monoclonal anti-FLAG antibody (1:1000,
954 #F3165, Sigma-Aldrich), mouse monoclonal anti-vinculin antibody (1:500, #MAB3574, EMD

955 Millipore), mouse monoclonal anti-TOMM20 antibody (1:1000, #sc-17764, Santa Cruz
956 Biotechnologies), mouse monoclonal anti-γ-tubulin antibody (1:1000, #T6557, Sigma-Aldrich)
957 and rabbit polyclonal anti-FLAG antibody (1:1000, #F7425, Sigma-Aldrich). Afterwards,
958 coverslips were washed three times in 1x PBS for 5 min and incubated with secondary
959 antibodies [donkey anti-rabbit Alexa594 (1:1000, #A21207, Invitrogen) and goat anti-mouse
960 Alexa488 (1:1000, #11029, Invitrogen)] diluted in 1x PBS including 1% pig or goat serum for
961 1h at RT. Then coverslips were washed 3x in 1x PBS (the first washing including DAPI DNA
962 dye) and mounted with Fluorsave reagent (Calibiochem). Transmission electron microscopy on
963 cells was performed as previously described (Gao et al, 2014).
964
965 **Microscopy and image analysis**
966 Immunofluorescence images were acquired with a spinning-disk confocal microscope
967 (UltraVIEW VoX, PerkinElmer) using a 60× objective. Images represent a single plane and
968 were deconvoluted using ImageJ (NIH) and brightness was adjusted equally in the entire
969 images. Specificity of the anti-CLUH antibody has been proven before (Pla-Martin et al, 2020).
970 For CLUH-granule quantification, at least 160 cells have been analyzed per genotype per
971 experiment and cells with CLUH-granules were counted manually with the experimentator
972 blinded for the genotype. For mitochondrial morphology assessment, a half-automated macro
973 for ImageJ (Mitomorph) has been employed (Yim et al, 2020). At least 66 (basal) or 44
974 (galactose) cells per genotype per experiment were analyzed. Micrographs were acquired on a
975 Jeol Jem2100Plus electron microscope operating at a voltage of 120 V using a GATAN
976 OneView camera.
977
978 **Propidium iodide staining and flow cytometry**
979 Cells were synchronized as described before (Figure 8A), collected by trypsinization and
980 pelleting, washed once with 1x PBS, fixed in ice-cold 70% ethanol in 1x PBS and stored at -

981 20°C for at least 16h. Fixed cells were pelleted at 2000 rpm for 10 min, washed once with 1x
982 PBS and pelleted again at 2000 rpm for 5 min. Pellets were resuspended in 500 µl 1x PBS
983 containing 0.25% Triton X-100, 100 µg/mL RNase A (#1007885, Qiagen) and 50 µg/mL PI
984 (#P4864, Sigma-Aldrich) and incubated at least 30 min at RT before measured by flow
985 cytometry. BD LSR Fortessa (BD Biosciences) was used with BD FACS Diva software at low
986 flow rate using PE laser (561 nm excitation; 586/15 nm detection). At least 15,000 events were
987 measured per sample. Flowing Software version 2.5.1 (developed by Perttu Terho, Turku
988 Centre for Biotechnology, University of Turku, Finland) was used for analysis.

989 **Statistics**

990 Sample size has been determined by previous experience with similar analysis. Replicates are
991 always biological independent experiments. Data are shown as mean ± SEM or ± SD as
992 indicated in respective figure legends. To compare two groups, paired or unpaired Student`s t-
993 test was performed as indicated in the figure legends. To compare multiple groups, one-way
994 ANOVA with post hoc Tukey`s multiple comparison test was performed. To compare data sets
995 including two variances, two-way ANOVA with post hoc Tukey's multiple comparison test
996 was employed. Statistical significance was calculated using GraphPad Prism software. A P
997 value < 0.05 was considered as significant. Statistical methods for proteomics analysis are
998 described in the corresponding method section.

999

ACKNOWLEDGMENTS

We are grateful to Guy Lenaers for providing *CLUH* knock-out HeLa cells, and to Iain Cheeseman for sharing the *SPAG5* and *KNSTRN* ind-KO cell lines. We thank the CECAD imaging and proteomics facilities for excellent technical assistance, and members of the Rugarli laboratory for constructive discussions. This work was funded by the Deutsche Forschungsgemeinschaft (Project numbers 269925409 and 411422114-GRK 2550) to E.I.R.

COMPETING INTERESTS

The authors declare no competing interests.

REFERENCES

Abdel-Fatah TMA, Agarwal D, Liu DX, Russell R, Rueda OM, Liu K, Xu B, Moseley PM, Green AR, Pockley AG, Rees RC, Caldas C, Ellis IO, Ball GR, Chan SYT (2016) SPAG5 as a prognostic biomarker and chemotherapy sensitivity predictor in breast cancer: a retrospective, integrated genomic, transcriptomic, and protein analysis. *Lancet Oncol* **17:** 1004-1018

Ahn E, Kumar P, Mukha D, Tzur A, Shlomi T (2017) Temporal fluxomics reveals oscillations in TCA cycle flux throughout the mammalian cell cycle. *Molecular Systems Biology* **13:** 953

Bertucci F, Viens P, Birnbaum D (2016) SPAG5: the ultimate marker of proliferation in early breast cancer? *Lancet Oncol* **17:** 863-865

Bruderer R, Bernhardt OM, Gandhi T, Miladinović SM, Cheng LY, Messner S, Ehrenberger T, Zanotelli V, Butscheid Y, Escher C, Vitek O, Rinner O, Reiter L (2015) Extending the limits of quantitative proteome profiling with data-independent acquisition and application to acetaminophen-treated three-dimensional liver microtissues. *Mol Cell Proteomics* **14:** 1400-1410

Buchakjian MR, Kornbluth S (2010) The engine driving the ship: metabolic steering of cell proliferation and death. *Nat Rev Mol Cell Bio* **11:** 715-727

Chang MS, Huang CJ, Chen ML, Chen ST, Fan CC, Chu JM, Lin WC, Yang YC (2001) Cloning and characterization of hMAP126, a new member of mitotic spindle-associated proteins. *Biochem Biophys Res Commun* **287:** 116-121

Chen EY, Tan CM, Kou Y, Duan Q, Wang Z, Meirelles GV, Clark NR, Ma'ayan A (2013) Enrichr: interactive and collaborative HTML5 gene list enrichment analysis tool. *BMC bioinformatics* **14:** 128

1038
1039 Cheng TS, Hsiao YL, Lin CC, Hsu CM, Chang MS, Lee CI, Yu RC, Huang CY, Howng SL, Hong YR
1040 (2007) hNinein is required for targeting spindle-associated protein Astrin to the centrosome during the
1041 S and G2 phases. *Exp Cell Res* **313:** 1710-1721

1042
1043 Cheng TS, Hsiao YL, Lin CC, Yu CT, Hsu CM, Chang MS, Lee CI, Huang CY, Howng SL, Hong YR
1044 (2008) Glycogen synthase kinase 3beta interacts with and phosphorylates the spindle-associated protein
1045 astrin. *J Biol Chem* **283:** 2454-2464

1046
1047 Chiu SC, Chen JM, Wei TY, Cheng TS, Wang YH, Ku CF, Lian CH, Liu CC, Kuo YC, Yu CT (2014)
1048 The mitosis-regulating and protein-protein interaction activities of astrin are controlled by aurora-A-
1049 induced phosphorylation. *Am J Physiol Cell Physiol* **307:** C466-478

1050
1051 Chung HJ, Park JE, Lee NS, Kim H, Jang CY (2016) Phosphorylation of Astrin Regulates Its
1052 Kinetochore Function. *J Biol Chem* **291:** 17579-17592

1053
1054 Cuyàs E, Corominas-Faja B, Joven J, Menendez JA (2014) Cell cycle regulation by the nutrient-sensing
1055 mammalian target of rapamycin (mTOR) pathway. *Methods Mol Biol* **1170:** 113-144

1056
1057 Dai LY, Zhao TY, Bisteau X, Sun WD, Prabhu N, Lim YT, Sobota RM, Kaldis P, Nordlund P (2018)
1058 Modulation of Protein-Interaction States through the Cell Cycle. *Cell* **173:** 1481-+

1059
1060 DeBerardinis RJ, Lum JJ, Hatzivassiliou G, Thompson CB (2008) The biology of cancer: Metabolic
1061 reprogramming fuels cell growth and proliferation. *Cell Metab* **7:** 11-20

1062
1063 Dunsch AK, Linnane E, Barr FA, Gruneberg U (2011) The astrin-kinastrin/SKAP complex localizes to
1064 microtubule plus ends and facilitates chromosome alignment. *The Journal of cell biology* **192:** 959-968

1065
1066 Dutchak PA, Estill-Terpack SJ, Plec AA, Zhao X, Yang C, Chen J, Ko B, Deberardinis RJ, Yu Y, Tu
1067 BP (2018) Loss of a Negative Regulator of mTORC1 Induces Aerobic Glycolysis and Altered Fiber
1068 Composition in Skeletal Muscle. *Cell Rep* **23:** 1907-1914

1069
1070 Friese A, Faesen AC, Huis in 't Veld PJ, Fischbock J, Prumbaum D, Petrovic A, Raunser S, Herzog F,
1071 Musacchio A (2016) Molecular requirements for the inter-subunit interaction and kinetochore
1072 recruitment of SKAP and Astrin. *Nat Commun* **7:** 11407

1073
1074 Gao J, Schatton D, Martinelli P, Hansen H, Pla-Martin D, Barth E, Becker C, Altmueller J, Frommolt
1075 P, Sardiello M, Rugarli EI (2014) CLUH regulates mitochondrial biogenesis by binding mRNAs of
1076 nuclear-encoded mitochondrial proteins. *J Cell Biol* **207:** 213-223

1077
1078 Geraghty Z, Barnard C, Uluocak P, Gruneberg U (2021) The association of Plk1 with the astrin–
1079 kinastrin complex promotes formation and maintenance of a metaphase plate. *J Cell Sci* **134**

1080
1081 Gholkar AA, Senese S, Lo Y-C, Vides E, Contreras E, Hodara E, Capri J, Whitelegge JP, Torres JZ
1082 (2016) The X-Linked-Intellectual-Disability-Associated Ubiquitin Ligase Mid2 Interacts with Astrin
1083 and Regulates Astrin Levels to Promote Cell Division. *Cell Rep* **14:** 180-188

1084

1085 Gruber J, Harborth J, Schnabel J, Weber K, Hatzfeld M (2002) The mitotic-spindle-associated protein
1086 astrin is essential for progression through mitosis. *J Cell Sci* **115:** 4053-4059

1087
1088 Halim VA, Alvarez-Fernandez M, Xu YJ, Aprelia M, van den Toorn HWP, Heck AJR, Mohammed S,
1089 Medema RH (2013) Comparative Phosphoproteomic Analysis of Checkpoint Recovery Identifies New
1090 Regulators of the DNA Damage Response. *Sci Signal* **6**

1091
1092 Halim VA, Garcia-Santisteban I, Warmerdam DO, van den Broek W, Heck AJR, Mohammed S,
1093 Medema RH (2018) Doxorubicin-induced DNA Damage Causes Extensive Ubiquitination of
1094 Ribosomal Proteins Associated with a Decrease in Protein Translation. *Molecular & Cellular*
1095 *Proteomics* **17:** 2297-2308

1096
1097 Harbauer AB, Opalinska M, Gerbeth C, Herman JS, Rao S, Schonfisch B, Guiard B, Schmidt O, Pfanner
1098 N, Meisinger C (2014) Cell cycle-dependent regulation of mitochondrial preprotein translocase. *Science*
1099 **346:** 1109-1113

1100
1101 Kern DM, Monda JK, Su KC, Wilson-Kubalek EM, Cheeseman IM (2017) Astrin-SKAP complex
1102 reconstitution reveals its kinetochore interaction with microtubule-bound Ndc80. *Elife* **6**

1103
1104 Kern DM, Nicholls PK, Page DC, Cheeseman IM (2016) A mitotic SKAP isoform regulates spindle
1105 positioning at astral microtubule plus ends. *J Cell Biol* **213:** 315-328

1106
1107 Khan NA, Nikkanen J, Yatsuga S, Jackson C, Wang L, Pradhan S, Kivela R, Pessia A, Velagapudi V,
1108 Suomalainen A (2017) mTORC1 Regulates Mitochondrial Integrated Stress Response and
1109 Mitochondrial Myopathy Progression. *Cell Metab* **26:** 419-428 e415

1110
1111 Kodani A, Yu TW, Johnson JR, Jayaraman D, Johnson TL, Al-Gazali L, Sztriha L, Partlow JN, Kim H,
1112 Krup AL, Dammermann A, Krogan NJ, Walsh CA, Reiter JF (2015) Centriolar satellites assemble
1113 centrosomal microcephaly proteins to recruit CDK2 and promote centriole duplication. *Elife* **4**

1114
1115 Koppen M, Metodiev MD, Casari G, Rugarli EI, Langer T (2007) Variable and Tissue-Specific Subunit
1116 Composition of Mitochondrial m-AAA Protease Complexes Linked to Hereditary Spastic Paraplegia.
1117 *Mol Cell Biol* **27:** 758-767

1118
1119 Kuleshov MV, Jones MR, Rouillard AD, Fernandez NF, Duan Q, Wang Z, Koplev S, Jenkins SL,
1120 Jagodnik KM, Lachmann A, McDermott MG, Monteiro CD, Gundersen GW, Ma'ayan A (2016)
1121 Enrichr: a comprehensive gene set enrichment analysis web server 2016 update. *Nucleic Acids Res* **44:**
1122 W90-97

1123
1124 Leal-Esteban LC, Fajas L (2020) Cell cycle regulators in cancer cell metabolism. *Bba-Mol Basis Dis*
1125 **1866**

1126
1127 Lee IH, Finkel T (2013) Metabolic regulation of the cell cycle. *Curr Opin Cell Biol* **25:** 724-729

1128
1129 Li M, Li A, Zhou S, Lv H, Yang W (2019) SPAG5 upregulation contributes to enhanced c-MYC
1130 transcriptional activity via interaction with c-MYC binding protein in triple-negative breast cancer.
1131 *Journal of hematology & oncology* **12:** 14

1132

1133 MacVicar T, Ohba Y, Nolte H, Mayer FC, Tatsuta T, Sprenger H-G, Lindner B, Zhao Y, Li J, Bruns C,
1134 Krüger M, Habich M, Riemer J, Schwarzer R, Pasparakis M, Henschke S, Brüning JC, Zamboni N,
1135 Langer T (2019) Lipid signalling drives proteolytic rewiring of mitochondria by YME1L. *Nature* **575:**
1136 361-365

1137
1138 Mandal S, Guptan P, Owusu-Ansah E, Banerjee U (2005) Mitochondrial Regulation of Cell Cycle
1139 Progression during Development as Revealed by the tenured Mutation in Drosophila. *Dev Cell* **9:** 843-
1140 854

1141
1142 Manning AL, Bakhoum SF, Maffini S, Correia-Melo C, Maiato H, Compton DA (2010) CLASP1, astrin
1143 and Kif2b form a molecular switch that regulates kinetochore-microtubule dynamics to promote mitotic
1144 progression and fidelity. *The EMBO journal* **29:** 3531-3543

1145
1146 McKinley KL, Cheeseman IM (2017) Large-Scale Analysis of CRISPR/Cas9 Cell-Cycle Knockouts
1147 Reveals the Diversity of p53-Dependent Responses to Cell-Cycle Defects. *Dev Cell* **40:** 405-420

1148
1149 Mitra K, Wunder C, Roysam B, Lin G, Lippincott-Schwartz J (2009) A hyperfused mitochondrial state
1150 achieved at G(1)-S regulates cyclin E buildup and entry into S phase. *Proc Natl Acad Sci U S A* **106:**
1151 11960-11965

1152
1153 Morita M, Gravel SP, Chenard V, Sikstrom K, Zheng L, Alain T, Gandin V, Avizonis D, Arguello M,
1154 Zakaria C, McLaughlan S, Nouet Y, Pause A, Pollak M, Gottlieb E, Larsson O, St-Pierre J, Topisirovic
1155 I, Sonenberg N (2013) mTORC1 Controls Mitochondrial Activity and Biogenesis through 4E-BP-
1156 Dependent Translational Regulation. *Cell Metab* **18:** 698-711

1157
1158 Morita M, Prudent J, Basu K, Goyon V, Katsumura S, Hulea L, Pearl D, Siddiqui N, Strack S, McGuirk
1159 S, St-Pierre J, Larsson O, Topisirovic I, Vali H, McBride HM, Bergeron JJ, Sonenberg N (2017) mTOR
1160 Controls Mitochondrial Dynamics and Cell Survival via MTFP1. *Mol Cell* **67:** 922-935 e925

1161
1162 Morris DR, Geballe AP (2000) Upstream open reading frames as regulators of mRNA translation. *Mol*
1163 *Cell Biol* **20:** 8635-8642

1164
1165 Nolte H, MacVicar TD, Tellkamp F, Kruger M (2018) Instant Clue: A Software Suite for Interactive
1166 Data Visualization and Analysis. *Sci Rep* **8**

1167
1168 Olsen JV, Vermeulen M, Santamaria A, Kumar C, Miller ML, Jensen LJ, Gnad F, Cox J, Jensen TS,
1169 Nigg EA, Brunak S, Mann M (2010) Quantitative phosphoproteomics reveals widespread full
1170 phosphorylation site occupancy during mitosis. *Sci Signal* **3:** ra3

1171
1172 Pla-Martin D, Schatton D, Wiederstein JL, Marx MC, Khiati S, Kruger M, Rugarli EI (2020) CLUH
1173 granules coordinate translation of mitochondrial proteins with mTORC1 signaling and mitophagy.
1174 *EMBO J* **39:** e102731

1175
1176 Rabanal-Ruiz Y, Byron A, Wirth A, Madsen R, Sedlackova L, Hewitt G, Nelson G, Stingele J, Wills
1177 JC, Zhang T, Zeug A, Fassler R, Vanhaesebroeck B, Maddocks ODK, Ponimaskin E, Carroll B,
1178 Korolchuk VI (2021) mTORC1 activity is supported by spatial association with focal adhesions. *J Cell*
1179 *Biol* **220**

1180

1181 Rappsilber J, Mann M, Ishihama Y (2007) Protocol for micro-purification, enrichment, pre-fractionation
1182 and storage of peptides for proteomics using StageTips. *Nat Protocols* **2:** 1896-1906

1183
1184 Salazar-Roa M, Malumbres M (2017) Fueling the Cell Division Cycle. *Trends Cell Biol* **27:** 69-81

1185
1186 Schatton D, Pla-Martin D, Marx MC, Hansen H, Mourier A, Nemazanyy I, Pessia A, Zentis P, Corona
1187 T, Kondylis V, Barth E, Schauss AC, Velagapudi V, Rugarli EI (2017) CLUH regulates mitochondrial
1188 metabolism by controlling translation and decay of target mRNAs. *J Cell Biol* **216:** 675-693

1189
1190 Schatton D, Rugarli EI (2018) A concert of RNA-binding proteins coordinates mitochondrial function.
1191 *Crit Rev Biochem Mol Biol* **53:** 652-666

1192
1193 Schmidt JC, Kiyomitsu T, Hori T, Backer CB, Fukagawa T, Cheeseman IM (2010) Aurora B kinase
1194 controls the targeting of the Astrin-SKAP complex to bioriented kinetochores. *J Cell Biol* **191:** 269-280

1195
1196 Schwaiger M, Rampler E, Hermann G, Miklos W, Berger W, Koellensperger G (2017) Anion-Exchange
1197 Chromatography Coupled to High-Resolution Mass Spectrometry: A Powerful Tool for Merging
1198 Targeted and Non targeted Metabolomics. *Anal Chem* **89:** 7667-7674

1199
1200 Thedieck K, Holzwarth B, Prentzell MT, Boehlke C, Klasener K, Ruf S, Sonntag AG, Maerz L,
1201 Grellscheid SN, Kremmer E, Nitschke R, Kuehn EW, Jonker JW, Groen AK, Reth M, Hall MN,
1202 Baumeister R (2013) Inhibition of mTORC1 by astrin and stress granules prevents apoptosis in cancer
1203 cells. *Cell* **154:** 859-874

1204
1205 Thein KH, Kleylein-Sohn J, Nigg EA, Gruneberg U (2007) Astrin is required for the maintenance of
1206 sister chromatid cohesion and centrosome integrity. *J Cell Biol* **178:** 345-354

1207
1208 Tyanova S, Temu T, Cox J (2016a) The MaxQuant computational platform for mass spectrometry-based
1209 shotgun proteomics. *Nat Protocols* **11:** 2301-2319

1210
1211 Tyanova S, Temu T, Sinitcyn P, Carlson A, Hein MY, Geiger T, Mann M, Cox J (2016b) The Perseus
1212 computational platform for comprehensive analysis of (prote)omics data. *Nat Meth* **13:** 731-740

1213
1214 Wakim J, Goudenege D, Perrot R, Gueguen N, Desquiret-Dumas V, Chao de la Barca JM, Dalla Rosa
1215 I, Manero F, Le Mao M, Chupin S, Chevrollier A, Procaccio V, Bonneau D, Logan DC, Reynier P,
1216 Lenaers G, Khiati S (2017) CLUH couples mitochondrial distribution to the energetic and metabolic
1217 status. *J Cell Sci* **130:** 1940-1951

1218
1219 Wang ZQ, Fan M, Candas D, Zhang TQ, Qin LL, Eldridge A, Wachsmann-Hogiu S, Ahmed KM,
1220 Chromy BA, Nantajit D, Duru N, He FC, Chen M, Finkel T, Weinstein LS, Li JJ (2014) Cyclin B1/Cdk1
1221 Coordinates Mitochondrial Respiration for Cell-Cycle G2/M Progression. *Dev Cell* **29:** 217-232

1222
1223 Wong JMT, Malec PA, Mabrouk OS, Ro J, Dus M, Kennedy RT (2016) Benzoyl chloride derivatization
1224 with liquid chromatography-mass spectrometry for targeted metabolomics of neurochemicals in
1225 biological samples. *J Chromatogr A* **1446:** 78-90

1226

1227 Xie Z, Bailey A, Kuleshov MV, Clarke DJB, Evangelista JE, Jenkins SL, Lachmann A, Wojciechowicz
1228 ML, Kropiwnicki E, Jagodnik KM, Jeon M, Ma'ayan A (2021) Gene Set Knowledge Discovery with
1229 Enrichr. *Current Protocols* **1:** e90

1230
1231 Yim A, Koti P, Bonnard A, Marchiano F, Dürrbaum M, Garcia-Perez C, Villaveces J, Gamal S, Cardone
1232 G, Perocchi F, Storchova Z, Habermann BH (2020) mitoXplorer, a visual data mining platform to
1233 systematically analyze and visualize mitochondrial expression dynamics and mutations. *Nucleic Acids*
1234 *Res* **48:** 605-632

1235
1236 Ying Z, Yang J, Li W, Wang X, Zhu Z, Jiang W, Li C, Sha O (2020) Astrin: A Key Player in Mitosis
1237 and Cancer. *Front Cell Dev Biol* **8:** 866-866

1238
1239 Young SK, Wek RC (2016) Upstream Open Reading Frames Differentially Regulate Gene-specific
1240 Translation in the Integrated Stress Response. *J Biol Chem* **291:** 16927-16935

1241
1242 Yuan LJ, Li JD, Zhang L, Wang JH, Wan T, Zhou Y, Tu H, Yun JP, Luo RZ, Jia WH, Zheng M (2014)
1243 SPAG5 upregulation predicts poor prognosis in cervical cancer patients and alters sensitivity to taxol
1244 treatment via the mTOR signaling pathway. *Cell Death Dis* **5:** e1247

1245
1246 Zhou H, Wang SC, Ma JM, Yu LQ, Jing JS (2018) Sperm-Associated Antigen 5 Expression Is Increased
1247 in Hepatocellular Carcinoma and Indicates Poor Prognosis. *Medical science monitor : international*
1248 *medical journal of experimental and clinical research* **24:** 6021-6028

1249

1250

1251
1252

1253 **SUPPLEMENTARY FIGURES**

1254

1255

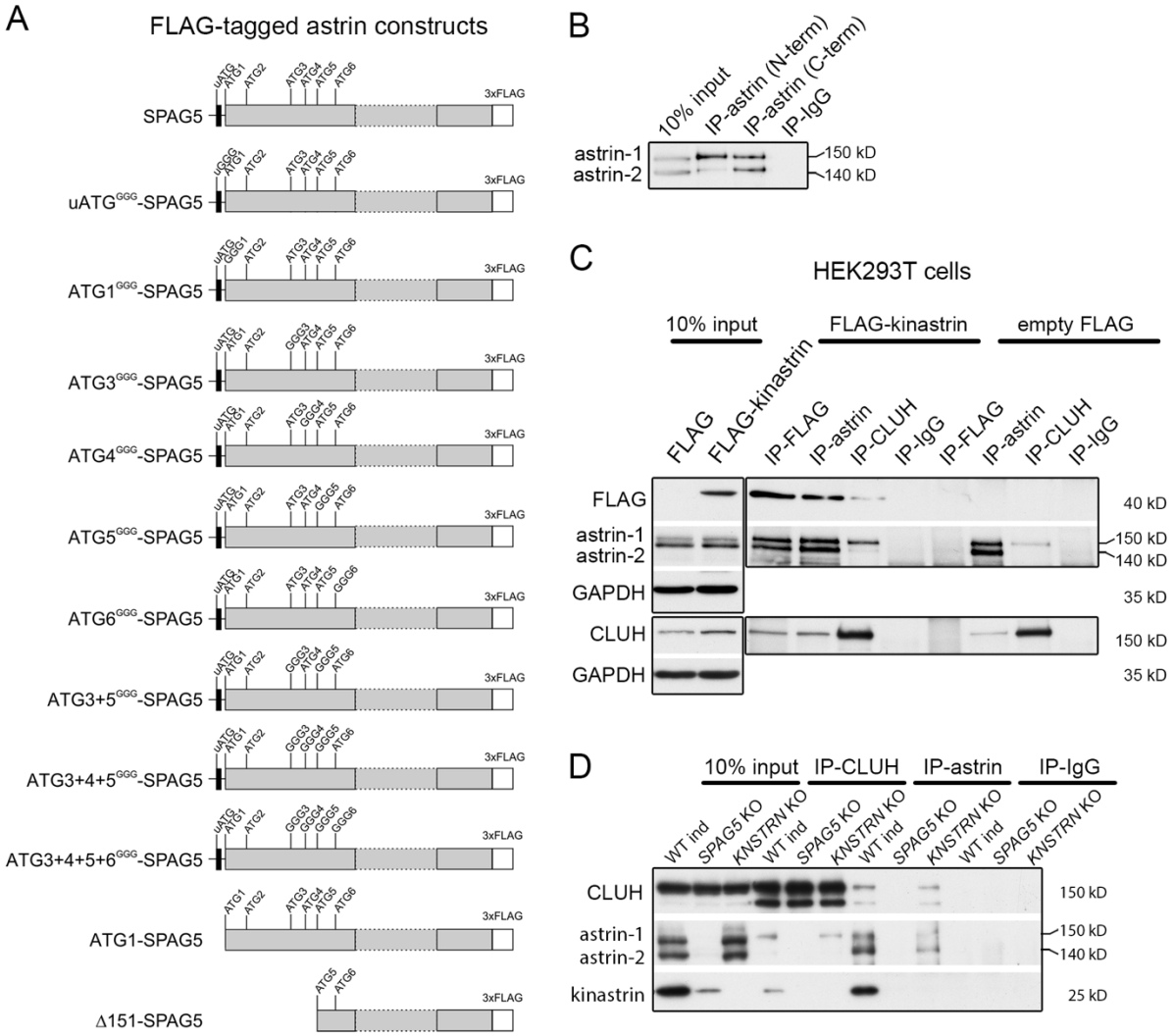

1256

1257

1258 **Figure 1-figure supplement 1. CLUH interacts with full length astrin independently of**
1259 **kinastrin.**

1260 (**A**) Scheme of C-terminally FLAG-tagged astrin constructs used for overexpression in this
1261 study. Positions of ATGs and mutagenized ATGs are indicated. (**B**) Western blot of IP of
1262 endogenous astrin using antibodies binding N-terminal or C-terminal epitopes of astrin in HeLa
1263 cells. (**C**) Western blots of reciprocal co-IPs in HEK293T cells stably overexpressing FLAG-
1264 kinastrin or empty FLAG using antibodies against endogenous CLUH, astrin and overexpressed
1265 kinastrin. GAPDH was used as loading control for input samples. (**D**) Western blots of
1266 reciprocal co-IPs of endogenous CLUH and astrin in WT, *SPAG5* and *KNSTRN* ind-KO HeLa
1267 cells.

1268

1269

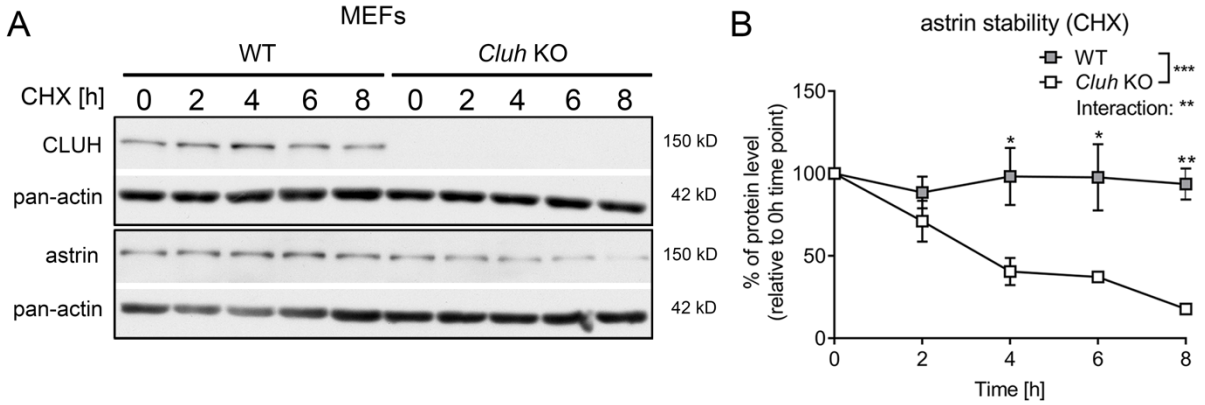

1270

1271 **Figure 2- figure supplement 1. Astrin is unstable in *Cluh* KO MEFs.**

1272 (**A**) Western blots of CHX chase in WT and *Cluh* KO MEFs treated for indicated time points.
1273 Pan-actin staining was used as loading control. (**B**) Quantification of CHX chase western blots
1274 as shown in A (n=3 independent experiments). Two-way ANOVA with post hoc Tukey`s
1275 multiple comparison test was performed with P≤0.05: *; P≤0.01: **; P≤0.001: ***. Genotype
1276 x time interaction significance is also shown. Graphs show mean ± SEM.

1277

1278

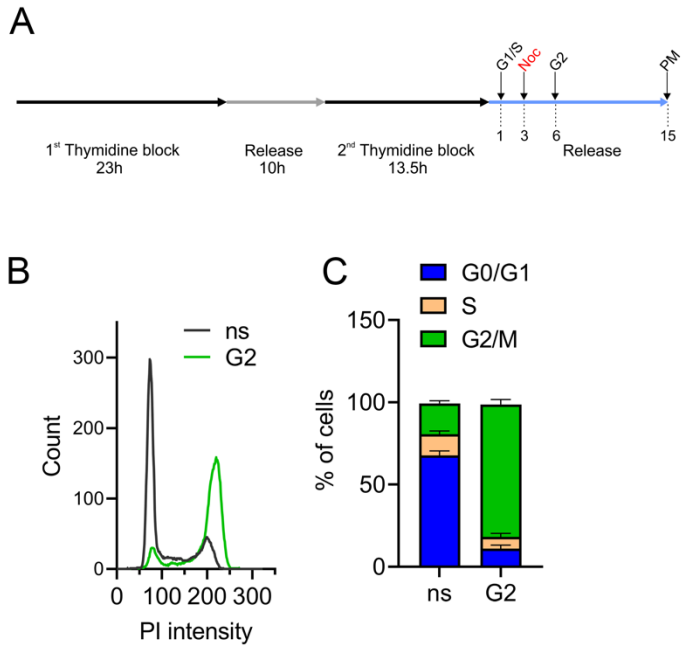

1279

1280 **Figure 3- figure supplement 1. Controls of effective synchronization of IP samples.**
1281 (**A**) Synchronization protocol used for IP experiments. Cells enriched in G1/S and G2 were
1282 collected after 1 h and 6 h after release of the 2nd thymidine block, respectively. Cells enriched
1283 in prometaphase (PM) were treated with nocodazole (noc) after 3 h of release and collected
1284 after additional 12 h. (**B, C**) PI intensity profiles (B) and cell cycle distribution analysis (C) of
1285 non-synchronized (ns) or G2-enriched WT cells used for IP followed by mass spectrometry
1286 (n=4 independent replicates).

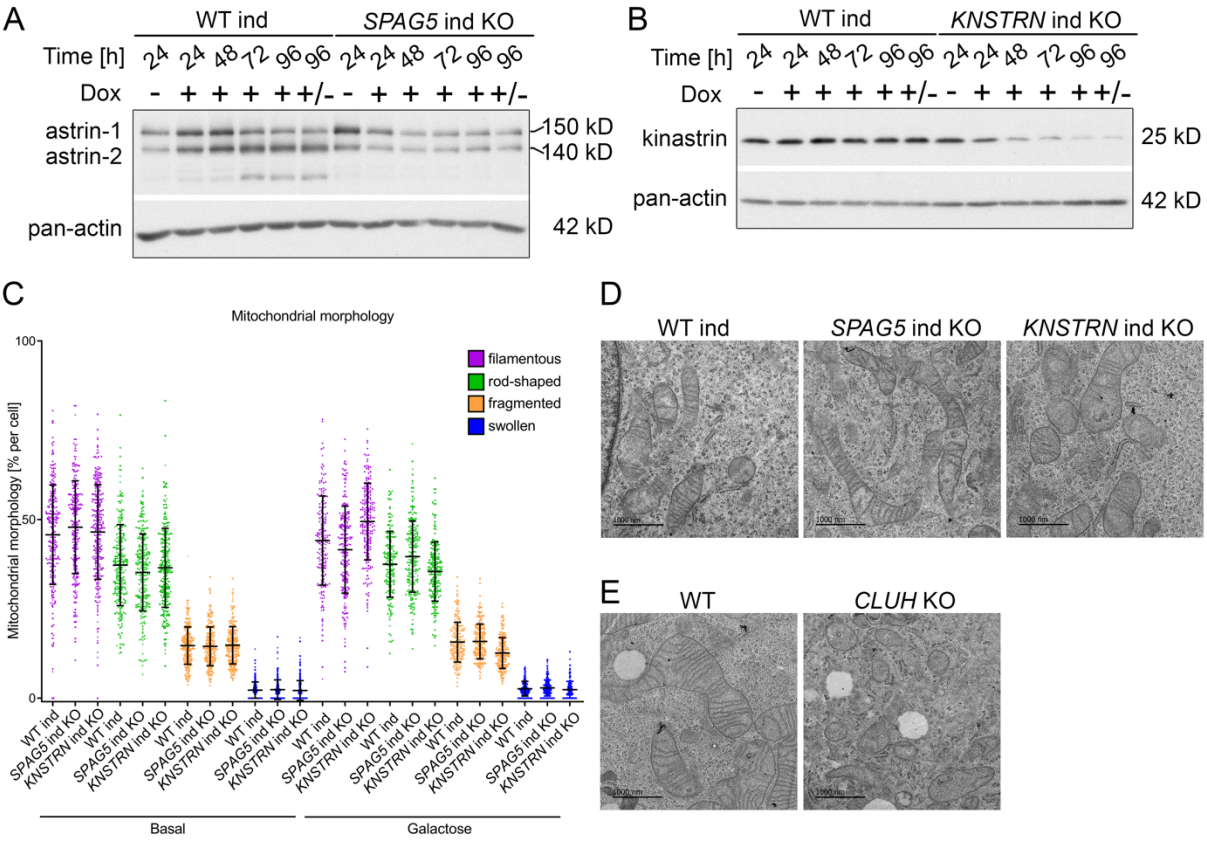

Figure 5-figure supplement 1. *SPAG5* and *KNSTRN* ind KO HeLa cells show normal mitochondrial morphology.

(**A, B**) Western blots of induction time course in WT and *SPAG5* (A) or *KNSTRN* (B) ind-KO HeLa cells. Cells were treated with doxycycline for indicated time points. +/- means that cells were treated with doxycycline for 72 h and not treated for the remaining 24 h. Pan-actin was used as loading control. (**C**) Quantification of mitochondrial morphology of experiments shown in Figure 5A (n=3 independent experiments; in total the following number of cells have been analyzed: basal: WT ind: 248, *SPAG5* ind KO: 244, *KNSTRN* ind KO: 274; galactose: WT ind: 186, *SPAG5* ind KO: 214, *KNSTRN* ind KO: 202). Scatter dots represent cells of all three replicates and symbols differ for cells belonging to different replicates. Graph shows mean ± SD. (**D, E**) Representative electron micrographs of WT, *SPAG5* and *KNSTRN* ind-KO (D) or WT and *CLUH* KO (E) HeLa cells. Scale bar, 1000 nm.

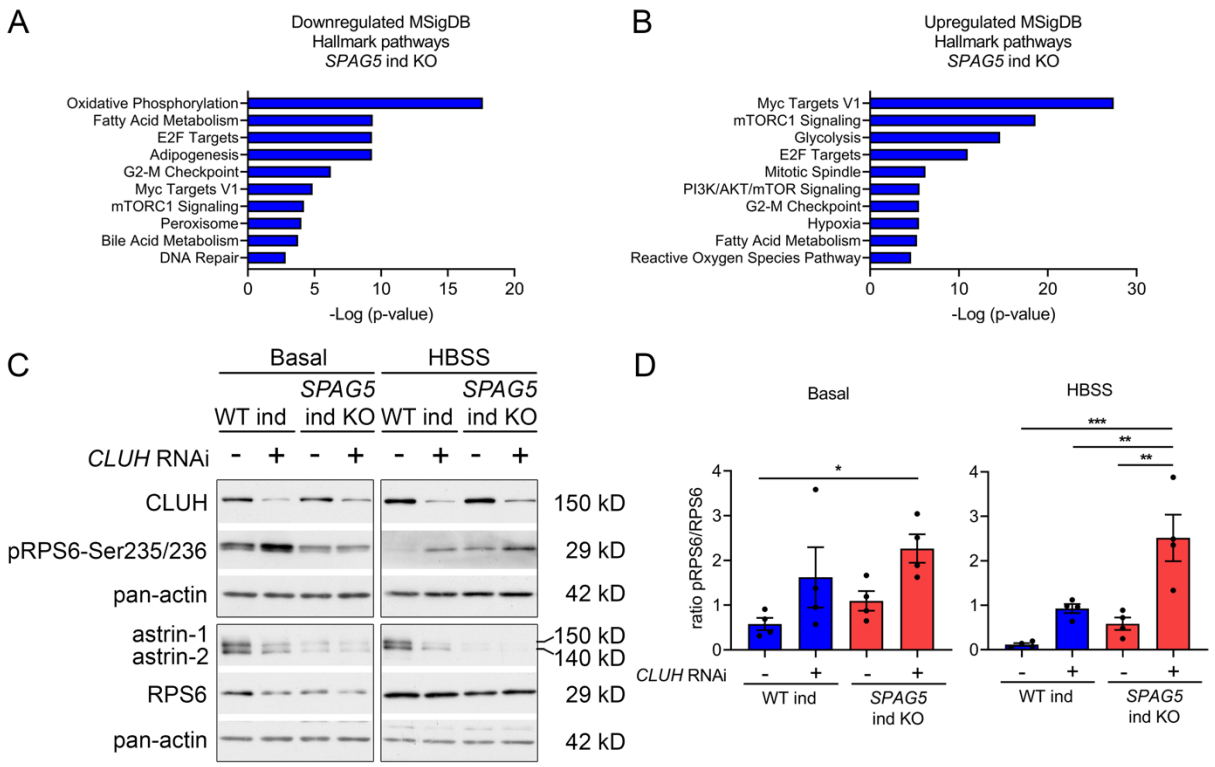

Figure 6-figure supplement 1. Loss of SPAG5 and CLUH lead to hyperactivation of mTORC1 signaling.

(**A, B**) MSigDB Hallmark pathways of downregulated (E) or upregulated (F) proteins (with a cut-off of p≤0.05; q≤0.15) detected in proteomics analysis of *SPAG5* ind-KO cells (Fig 4A and Supplementary Table3) using the EnrichR webtool. (**C**) Western blots of WT and *SPAG5* ind-KO HeLa cells transfected with siRNA against CLUH or untargeted control siRNA. Cells were induced for four days with doxycycline, additionally downregulated for the last three days and grown for the last 8 h in basal or HBSS media without doxycycline. Pan-actin was used as loading control. (**D**) Quantification of experiments as shown in C (n=4 independent experiments). Antibody signal was normalized to pan-actin signal, and signal of phospho-protein was normalized to signal of the total protein. Bars show mean ± SEM and dots represent values of individual replicates. One-way ANOVA with post hoc Tukey`s multiple comparison tests were performed with P≤0.05: *; P≤0.01: **; P≤0.001: ***.

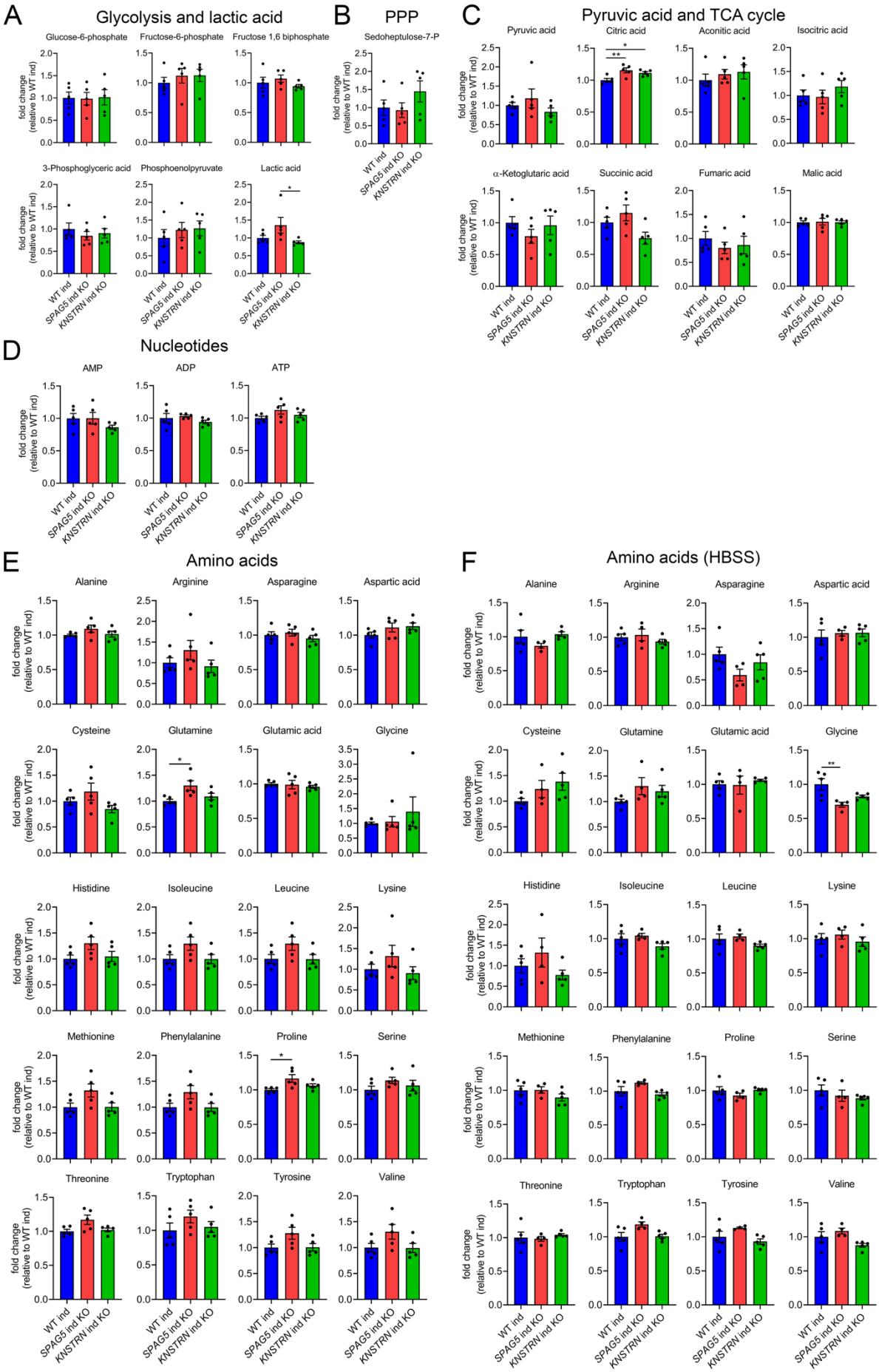
A
Glycolysis and lactic acid
Glucose-6-phosphate
Fructose-6-phosphate
Fructose 1,6 biphosphate
3-Phosphoglyceric acid
Phosphoenolpyruvate
Lactic acid
B
PPP
Sedoheptulose-7-P
C
Pyruvic acid and TCA cycle
Pyruvic acid
Citric acid
Aconitic acid
Isocitric acid
α-Ketoglutaric acid
Succinic acid
Fumaric acid
Malic acid
D
Nucleotides
AMP
ADP
ATP
E
Amino acids
Alanine
Arginine
Asparagine
Aspartic acid
Cysteine
Glutamine
Glutamic acid
Glycine
Histidine
Isoleucine
Leucine
Lysine
Methionine
Phenylalanine
Proline
Serine
Threonine
Tryptophan
Tyrosine
Valine
F
Amino acids (HBSS)
fold change (relative to WT ind)
WT ind
SPAG5 ind KO
KNSTRN ind KO

1317

1318 **Figure 6-figure supplement 2. Astrin and kinastrin depletion does not affect cellular**
1319 **metabolism under basal conditions.**
1320 (**A-F**) Targeted metabolomics of WT, *SPAG5* and *KNSTRN* ind-KO HeLa cells under basal
1321 conditions (A-E) or after 8h HBSS starvation (F) showing glycolytic intermediates and lactic
1322 acid (A), sedoheptulose-7-P (B), pyruvic acid and TCA cycle intermediates (C), nucleotide (D)
1323 and amino acid levels (E-F). Bars show mean ± SEM and dots represent values of individual
1324 replicates. One-way ANOVA with post hoc Tukey`s multiple comparison tests were performed
1325 on log converted fold changes with $P \leq 0.05$: *; $P \leq 0.01$: **.
1326

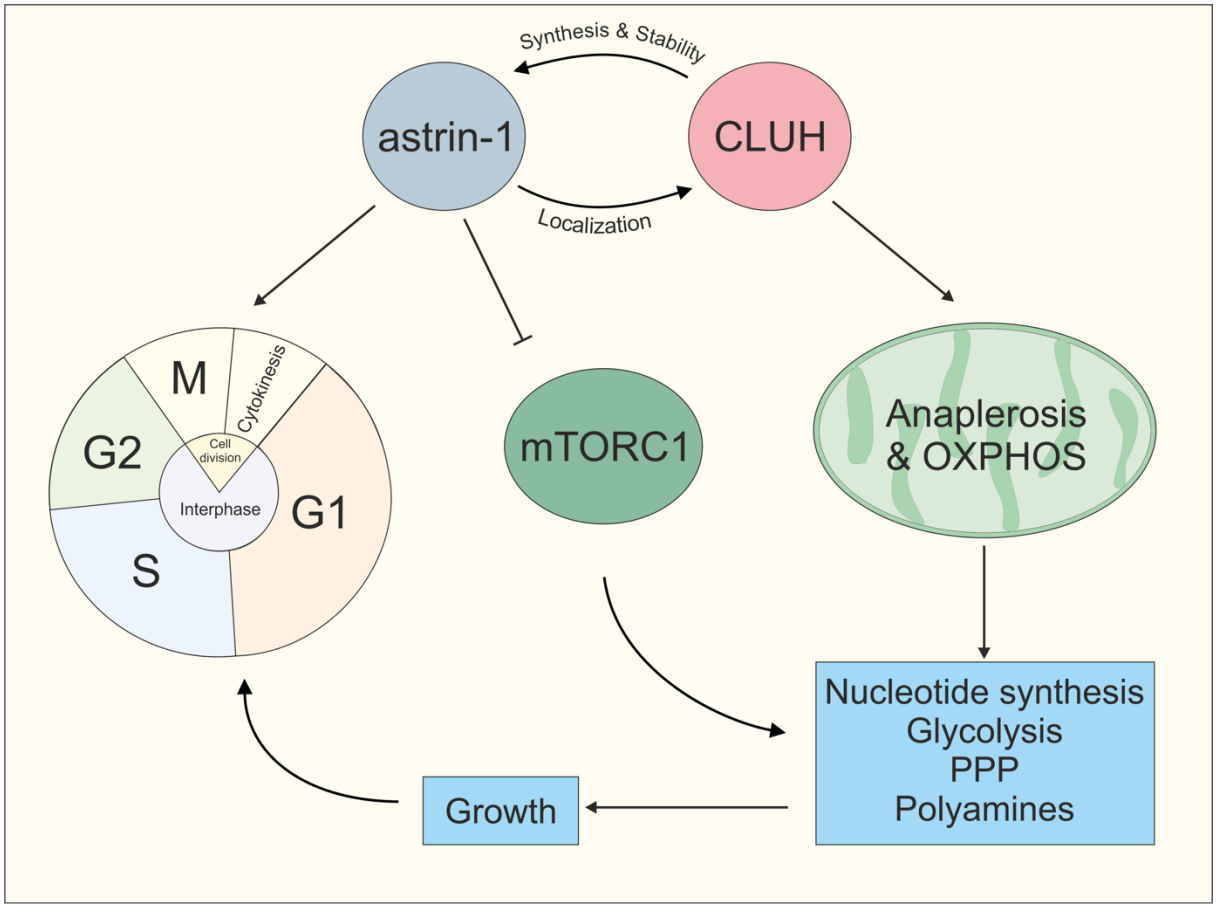

Figure 8- figure supplement 1. Model of CLUH/astrin-1 complex function in proliferating cells.

CLUH and astrin-1 form a complex and regulate each other reciprocally. On the one hand, CLUH is required for astrin synthesis and for protein stability. Additionally, CLUH promotes mitochondrial anaplerotic reactions and OXPHOS function by ensuring CLUH-target expression. This provides energy and building blocks to increase anabolic pathways like nucleotide synthesis, glycolysis, pentose phosphate pathway and polyamine synthesis required for growth in G1 and allowing cell cycle progression at the G1/S boundary. Astrin-1 on the other hand regulates CLUH localization, controls metaphase to anaphase progression in M phase and inhibits mTORC1.

1347
1348 ## SUPPLEMENTARY TABLES
1349
1350
1351 **Supplementary Table 1: Interactors of endogenous human CLUH in HeLa cells after**
1352 **SILAC labeling**
1353
1354
1355 **Supplementary Table 2: Interactors of endogenous human CLUH in G2-enriched HeLa**
1356 **cells**
1357
1358
1359 **Supplementary Table 3: Proteomics data of *SPAG5* and *KNSTRN* ind-KO HeLa cells**
1360
1361
1362 **Supplementary Table 4: IC-TQ_Transitions compound list**

1363

1364 **SOURCE DATA**
1365
1366
1367 **Figure 1-source data 1.** Uncropped blots for Figure 1A
1368
1369 **Figure 1-source data 2.** Uncropped blots for Figure 1B
1370
1371 **Figure 1-source data 3.** Uncropped blots for Figure 1D
1372
1373 **Figure 1-source data 4.** Uncropped blots for Figure 1E
1374
1375 **Figure 1-source data 5.** Uncropped blots for Figure 1F
1376
1377 **Figure 1-source data 6.** Uncropped blots for Figure 1G
1378
1379 **Figure 1-figure supplement 1-source data 1.** Uncropped blots for Figure 1-figure
1380 supplement 1B
1381
1382 **Figure 1-figure supplement 1-source data 2.** Uncropped blots for Figure 1-figure
1383 supplement 1C
1384
1385 **Figure 1-figure supplement 1-source data 3.** Uncropped blots for Figure 1-figure
1386 supplement 1D
1387
1388 **Figure 2-source data 1.** Uncropped blots for Figure 2A
1389
1390 **Figure 2-source data 2.** Uncropped blots for Figure 2H
1391
1392 **Figure 2-figure supplement 1-source data 1.** Uncropped blots for Figure 2-figure
1393 supplement 1A
1394

Figure 3-source data 1. Uncropped blots for Figure 3A

Figure 4-source data 1. Uncropped blots for Figure 4D

Figure 5-source data 1. Uncropped blots for Figure 5D

Figure 5-figure supplement 1-source data 1. Uncropped blots for Figure 5-figure supplement 1A

Figure 5-figure supplement 1-source data 2. Uncropped blots for Figure 5-figure supplement 1B

Figure 6-figure supplement 1-source data 1. Uncropped blots for Figure 6-figure supplement 1C

Figure 8-source data 1. Uncropped blots for Figure 8F